Commun. Comput. Phys.
doi: 10.4208/cicp.OA-2023-0053

Vol. **34**, No. 1, pp. 65-93
July 2023

Fast-Converging and Asymptotic-Preserving Simulation of Frequency Domain Thermoreflectance

Jia Liu[1] and Lei Wu[1,*]

[1] *Department of Mechanics and Aerospace Engineering, Southern University of Science and Technology, Shenzhen 518055, P.R. China.*

Communicated by Kun Xu

Received 24 February 2023; Accepted (in revised version) 6 May 2023

Abstract. The heat conduction under fast external excitation exists in many experiments measuring the thermal conductivity in solids, which is described by the phonon Boltzmann equation, i.e., the Callaway's model with dual relaxation times. Such a kinetic system has two spatial Knudsen numbers related to the resistive and normal scatterings, and one temporal Knudsen number determined by the external oscillation frequency. Thus, it is a challenge to develop an efficient numerical method. Here we first propose the general synthetic iterative scheme (GSIS) to solve the phonon Boltzmann equation, with the fast-converging and asymptotic-preserving properties: (i) the solution can be found within dozens of iterations for a wide range of Knudsen numbers and frequencies, and (ii) the solution is accurate when the spatial cell size in the bulk region is much larger than the phonon mean free path. Then, we investigate how the heating frequency affects the heat conduction in different transport regimes.

AMS subject classifications: 80M20

Key words: Frequency domain thermoreflectance, phonon Boltzmann equation, general synthetic iterative scheme.

1 Introduction

The heat conduction is critically important to the functionality and reliability of materials and devices, which is usually described by the Fourier conduction law, i.e., the heat flux ($\boldsymbol{q}$) is proportional to the product of negative temperature gradient ($-\nabla T$) and thermal conductivity (κ). However, numerous non-Fourier phenomena [1,2] have been observed

*Corresponding author. *Email addresses:* 12132407@mail.sustech.edu.cn (J. Liu), wul@sustech.edu.cn (L. Wu)

in either nanostructured materials (e.g., heat dissipation on chip cooling [3], thermoelectric energy conversion [4], and nanomedicine [5]) or ultrafast process [6, 7], which pose great challenges in investigating thermal properties of solid materials, especially when the ultrafast laser-based thermoreflectance techniques, including the time-domain thermoreflectance (TDTR) and the frequency-domain thermoreflectance (FDTR) techniques, are adopted.

Ultrafast thermoreflectance techniques often employ subpicosecond lasers [9]. Repeated laser pulses are divided into two beams, where the pump beam thermally excites a sample surface and the probe beam measures the time-resolved reflectivity or diffraction. In TDTR method, probe beam arrives at the sample surface at different time intervals after the pump beam through a mechanical delay stage. Various thermal properties, such as the cross-plane thermal conductivity, in-plane thermal conductivity, interfacial thermal conductance, and heat capacity, can be evaluated by fitting the temporal decay of measured signals to a thermal transport model, with unknown thermal properties as the fitting parameters. The TDTR technique has been applied to measure the thermal properties of thin films [10], multilayers [11], bulk materials [12], and their interfaces [13]. However, imperfections of the mechanical moving stage can introduce measurement errors, and ultrafast pulsed lasers are expensive. FDTR [7] is a variation of TDTR, where the thermoreflectance signals are measured by varying the modulation frequency of the pump beam instead of the delay time between the pump beam and the probe beams. FDTR can measure the same thermal properties as TDTR without a moving stage and ultrafast pulsed laser, thus eliminating the disadvantages of TDTR. There are two possible experimental setups for FDTR: one is based on pulsed lasers, almost the same setup as TDTR, with the modulation frequency ranging from 0.1 MHz to 80 MHz. In continuous-wave laser FDTR, the frequency of the pump beam is modulated by the electro-optical modulator and generates heat flux on the sample surface. Because it is not necessary to use an ultrafast pulsed laser, the continuous-wave laser FDTR can be configured at a low cost. Theoretically, in contrast to pulsed TDTR/FDTR, a pump beam of continuous-wave laser FDTR can be modulated at an infinite frequency. However, in practice, the modulation frequency is limited to less than 80 MHz due to the decreasing signal intensity and the presence of noise at high frequencies. To investigate the size effect of the thermal conductivity in nanoscale materials, wide-range modulation of the heating frequency is needed. Broadband FDTR has been implemented to overcome this frequency limitation and extend it to 200 MHz using heterodyne detection [8, 14], seeing the schematics in Fig. 1.

Note that the diffusion model based on the Fourier law is often used to extract the thermal conductivity from the experimental data. However, as the problem involves multiscale spatial-temporal heat transfer, the macroscopic conduction model cannot capture the dynamic thermal properties; meanwhile, mainstream methods, such as the molecular dynamics and non-equilibrium Green functions are computationally expensive. Thus, the mesoscopic method based on the phonon Boltzmann equation (PBE), which bridges the microscopic and macroscopic dynamics of heat carriers (phonon), shows great advan-

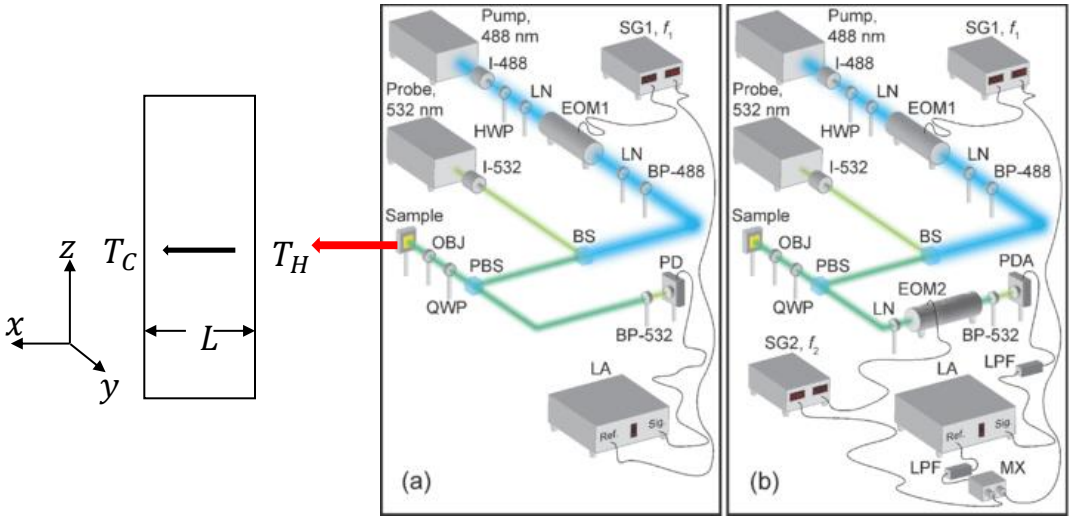

Figure 1: (a) Schematic of traditional FDTR. (b) Schematic of Broadband frequency-domain thermoreflectance technique [8]. An intensity modulated pump laser (488 nm) periodically heats the sample surface at a frequency f_1, a probe laser (532 nm) monitors the resultant thermal wave, and the phase lag of temperature (probe) to heat flux (pump) is monitored by a lock-in amplifier to determine the thermal properties.

tages [15–17]. The PBE is an integro-differential equation defined in the phase space of seven dimensions [18, 19]. The commonly used simplified models are single-relaxation-time model [19] and Callaway model [20]; the former works well when the resistive scattering (conserving energy but not momentum) dominates the heat conduction, such as in silicon and germanium. In low-dimensional materials or at extremely low temperatures, the normal scattering (conserving both energy and momentum) cannot be neglected, and the Callaway model should be more appropriate.

There are two main methods to find PBE solutions. The first method is the derivation of macroscopic equations, e.g., the ballistic-diffusive heat equations to capture the non-diffusive nature of phonons [21, 22] and the Guyer-Krumhansl equations when the normal scattering dominates [23]. However, these macroscopic equations cannot describe the heat conduction in all phonon transport regimes. The second method is the direct numerical simulation, such as the Monte Carlo scheme [24, 25], the discrete ordinate method [26, 27], and the discrete unified gas kinetic scheme [28, 29]. For time-dependent problems, the choice of time step is critical to above approaches. The widely used explicit time-marching strategy suffers difficulties when the problem strongly varies in physical space, because the spatial grid has to be small enough to capture the variation in a small spatial scale; the time step is limited by the smallest spatial cell size to ensure numerical stability. Consequently, implicit time-marching approaches to remove the restriction from the Courant-Friedrichs-Lewy condition are highly demanded. The conventional it-

erative scheme (CIS) serves this purpose, which is powerful in solving steady-state problems, but for physical problems with fast time variations (e.g., in TDTR/FDTR with high heating frequency) its advantage over explicit time-marching method might be not significant.

Fortunately, in FDTR the signal is small so that the system can be linearized around the equilibrium state. This means that the physical quantities vary with the external excitation periodically at the same frequency. Thus, the temporal variable can be eliminated in the PBE, and the problem becomes "periodic steady" with the frequency term added. It is well known that the CIS is quite inefficient for small Knudsen numbers, and the GSIS has been proposed to simulate the standard steady-state problems without external heating frequency excitation, which greatly accelerates the convergence of CIS [30]. The slow convergence of CIS also exists in the "periodic steady" problem. Additionally, we can see that the temperature profile varies intensively in spatial space as frequency increases in Fig. 6, which requires more spatial grids for CIS to capture the resolution, thus bringing great computational consumptions. With the fast-converging and asymptotic-preserving properties, it is natural and valuable to extend the GSIS to solve the FDTR problem to achieve fast convergence at all frequencies and Knudsen numbers with fewer spatial grids. It is noted that the external heating frequency makes great differences to standard steady-state problems, and it is the first time to use GSIS to systematically investigate the frequency effect on algorithm performance and conduction phenomena.

The remainder of this paper is organized as follows. In Section 2, the PBE in the "periodic steady" state is derived. In Section 3, the algorithm procedure is presented, and analytical Fourier analysis is performed to demonstrate the efficiency of GSIS.The fast-converging and asymptotic-preserving properties are confirmed by several numerical examples in Sections 4 and 5, respectively. In Section 6, we discuss the frequency effect on heat conduction systematically. Conclusions are given in Section 7.

2 Formulation of the problem

We consider the heat conduction across a slab with periodic plane-source heating on the surfaces, as shown in Fig. 1. The surface temperature depends on time t through

$$T_H = T_0 + \mathrm{Re}[\Delta T \exp(\mathtt{i}\omega t)], \quad T_C = T_0 - \mathrm{Re}[\Delta T \exp(\mathtt{i}\omega t)], \tag{2.1}$$

where $\mathtt{i}$ is the imaginary unit, Re denotes the real part of a complex variable, ΔT is a small quantity describing the temperature deviation from the equilibrium temperature T_0 (i.e., $|\Delta T| \ll T_0$). The heat conduction is modeled by the linearized PBE [20, 30]:

$$\frac{\partial f}{\partial t} + \boldsymbol{v}\cdot\boldsymbol{\nabla}_{\boldsymbol{x}} f = \frac{f_{eq}^R - f}{\tau_R} + \frac{f_{eq}^N - f}{\tau_N}, \tag{2.2}$$

where f is the phonon distribution function, t is the time, $\boldsymbol{x}$ is the spatial coordinate, and $\boldsymbol{v}$ is the phonon group velocity. While τ_R and τ_N are the relaxation time of the resis-

tive and normal scatterings, respectively, f_{eq}^R and f_{eq}^N are the corresponding equilibrium distributions:

$$f_{eq}^R=\frac{C_v(T-T_0)}{4\pi},\quad f_{eq}^N=\frac{C_v(T-T_0)}{4\pi}+\frac{C_vT\boldsymbol{u}\cdot\boldsymbol{s}}{4\pi|\boldsymbol{v}|}. \tag{2.3}$$

Here, C_v is the volumetric specific heat capacity, $\boldsymbol{s}=(\cos\theta,\sin\theta\cos\varphi,\sin\theta\sin\varphi)$ is the unit vector along the direction of $\boldsymbol{v}$, $\boldsymbol{u}$ is the drifted velocity. When the phonon distribution function is known, the macroscopic quantities can be calculated as $T-T_0=\frac{1}{C_v}\int f\mathrm{d}\Omega$, $\boldsymbol{q}=\int\boldsymbol{v}f\mathrm{d}\Omega$, $\boldsymbol{u}=\frac{3\boldsymbol{q}}{C_vT}$, Ω is the solid angle of scattering ($\mathrm{d}\Omega=\sin\theta\mathrm{d}\theta\mathrm{d}\varphi$).

Introducing the following dimensionless variables,

$$\begin{aligned}&\tilde{t}=\frac{t}{L/|\boldsymbol{v}|},\quad \tilde{x}=\frac{x}{L},\quad \tilde{\boldsymbol{v}}=\frac{\boldsymbol{v}}{|\boldsymbol{v}|},\quad \tilde{\boldsymbol{u}}=\frac{\boldsymbol{u}}{|\boldsymbol{v}|},\quad \tilde{T}=\frac{T-T_0}{\Delta T},\quad \tilde{\boldsymbol{q}}=\frac{\boldsymbol{q}}{C_v|\boldsymbol{v}|\Delta T},\\&\tilde{f}=\frac{f}{C_v\Delta T},\quad \tilde{f}_{eq}^R=\frac{f_{eq}^R}{C_v\Delta T},\quad \tilde{f}_{eq}^N=\frac{f_{eq}^N}{C_v\Delta T},\quad Kn_R=\frac{|\boldsymbol{v}|\tau_R}{L},\quad Kn_N=\frac{|\boldsymbol{v}|\tau_N}{L},\end{aligned} \tag{2.4}$$

Eq. (2.2) can be normalized as

$$\frac{\partial\tilde{f}}{\partial\tilde{t}}+\tilde{\boldsymbol{v}}\cdot\boldsymbol{\nabla}_{\tilde{x}}\tilde{f}=\frac{\tilde{f}_{eq}^R-\tilde{f}}{Kn_R}+\frac{\tilde{f}_{eq}^N-\tilde{f}}{Kn_N}, \tag{2.5}$$

with the dimensionless equilibrium distribution functions

$$\tilde{f}_{eq}^R=\frac{\tilde{T}}{4\pi},\quad \tilde{f}_{eq}^N=\frac{\tilde{T}}{4\pi}+\frac{3\tilde{\boldsymbol{q}}\cdot\tilde{\boldsymbol{v}}}{4\pi}, \tag{2.6}$$

and the dimensionless macroscopic quantities

$$\tilde{T}=\int\tilde{f}\mathrm{d}\Omega,\quad \tilde{\boldsymbol{q}}=\int\tilde{\boldsymbol{v}}\tilde{f}\mathrm{d}\Omega,\quad \tilde{\boldsymbol{u}}=3\tilde{\boldsymbol{q}}. \tag{2.7}$$

Under the periodic excitation (2.1), after sufficiently long time evolution, the time-dependent periodic heat conduction has the same frequency ω as the boundary temperature. Moreover, the translational symmetry of the planner heating eliminates the y and z spatial coordinates from consideration, so this problem is quasi-one-dimensional by expressing the distribution function as

$$\tilde{f}(\tilde{t},\tilde{x},\tilde{v})=\mathrm{Re}\left[\exp(\mathtt{i}\tilde{\omega}\tilde{t})\tilde{h}(\tilde{x},\tilde{v})\right], \tag{2.8}$$

where $\tilde{\omega}=\omega L/|\boldsymbol{v}|$, $\tilde{v}=\cos\theta$, and θ is the angle between the group velocity and the x-axis. Substituting Eq. (2.8) into Eq. (2.5), the time is eliminated, resulting in

$$\tilde{v}\frac{\partial\tilde{h}}{\partial\tilde{x}}=\frac{\tilde{h}_{eq}^R-\tilde{h}}{Kn_R}+\frac{\tilde{h}_{eq}^N-\tilde{h}}{Kn_N}-\mathtt{i}\tilde{\omega}\tilde{h}, \tag{2.9}$$

$\tilde{h}_{eq}^R$ and $\tilde{h}_{eq}^N$ are defined as

$$\tilde{h}_{eq}^R=\frac{\tilde{T}_h}{4\pi},\quad \tilde{h}_{eq}^N=\frac{\tilde{T}_h}{4\pi}+\frac{3\tilde{q}_h\tilde{v}}{4\pi}, \tag{2.10}$$

and

$$\tilde{T}_h=\int\tilde{h}\mathrm{d}\Omega=2\pi\int_{-1}^{1}\tilde{h}\mathrm{d}\tilde{v},\quad \tilde{\boldsymbol{q}}_h=\int\tilde{v}\tilde{h}\mathrm{d}\Omega=2\pi\int_{-1}^{1}\tilde{v}\tilde{h}\mathrm{d}\tilde{v}. \tag{2.11}$$

The thermalization boundary condition is employed as

$$\begin{cases}\tilde{h}(\tilde{v}>0,\tilde{x}=0)=\dfrac{\tilde{f}_{eq}^R(\tilde{T}_H)}{\exp(\mathrm{i}\tilde{\omega}\tilde{t})}=\dfrac{1}{4\pi},\\ \tilde{h}(\tilde{v}<0,\tilde{x}=1)=\dfrac{\tilde{f}_{eq}^R(\tilde{T}_C)}{\exp(\mathrm{i}\tilde{\omega}\tilde{t})}=-\dfrac{1}{4\pi}.\end{cases} \tag{2.12}$$

Once the converged solutions $\tilde{T}_h$ and $\tilde{q}_h$ obtained, we can determine the dimensionless temperature $\tilde{T}$ and heat flux $\tilde{q}$ as follows:

$$\tilde{T}(\tilde{x})=\mathrm{Re}\left[\exp(\mathrm{i}\tilde{\omega}\tilde{t})\int\tilde{h}\mathrm{d}\Omega\right]=\mathrm{Re}\left[\exp(\mathrm{i}\tilde{\omega}\tilde{t})\tilde{T}_h(\tilde{x})\right], \tag{2.13}$$

$$\tilde{q}(\tilde{x})=\mathrm{Re}\left[\exp(\mathrm{i}\tilde{\omega}\tilde{t})\int\tilde{v}\tilde{h}\mathrm{d}\Omega\right]=\mathrm{Re}[\exp(\mathrm{i}\tilde{\omega}\tilde{t})\tilde{q}_h(\tilde{x})]. \tag{2.14}$$

Generally speaking, $\tilde{T}_h$ and $\tilde{q}_h$ are complex variables, with their phase angle denoting the phase lag with respect to those at the solid surface.

3 Numerical scheme

In this section, we propose the GSIS to solve the linearized PBE and analytically analyze the efficiency of both GSIS and CIS via the Fourier stability analysis.

3.1 Basic idea of GSIS

The PBE is usually solved by CIS as shown in Eq. (3.6), where the scattering operator is split into the gain and loss terms. The advection operator and loss term are calculated at the current iteration step, while the gain term is evaluated at the previous iteration step, thus delaying the update of information. When the Knudsen number Kn_R and Kn_N are large, the gain term has little influence, while for small Knudsen numbers, the propagation of information (e.g., external excitation from the boundary) is inefficient for strong phonon scattering. This is why the CIS is efficient for large Knudsen numbers but costly in either diffusive or hydrodynamic regime. In order to enhance the information exchange across the whole computational domain, that is, to reduce the number of iteration

steps, the synthetic equations for the evolution of macroscopic variables that are asymptotic preserving the Fourier conduction equation in diffusive limit and Guyer-Krumhansl equation in hydrodynamic limit should be designed. The macroscopic variables solved from synthetic equations are more accurate than those of previous iteration step, which are then used in PBE to guide the evolution of distribution function to allow rapid propagation of perturbations to the global field.

To this end, we first multiply Eq. (2.9) by 2π, $2\pi\tilde{v}$, $2\pi\tilde{v}^2$, respectively, and integrating the resultant equations with respect to $\tilde{v}$, the following macroscopic synthetic equations are obtained:

$$\frac{\partial \tilde{q}_h}{\partial \tilde{x}} = -\mathtt{i}\tilde{\omega}\tilde{T}_h, \tag{3.1}$$

$$\frac{1}{3}\frac{\partial \tilde{T}_h}{\partial \tilde{x}} + \frac{\partial \tilde{N}_h}{\partial \tilde{x}} = -\left(\frac{1}{Kn_R} + \mathtt{i}\tilde{\omega}\right)\tilde{q}_h, \tag{3.2}$$

$$\frac{4}{15}\frac{\partial \tilde{q}_h}{\partial \tilde{x}} + \frac{\partial \tilde{M}_h}{\partial \tilde{x}} = -\left(\frac{1}{Kn_C} + \mathtt{i}\tilde{\omega}\right)\tilde{N}_h, \tag{3.3}$$

where $Kn_C^{-1} = Kn_R^{-1} + Kn_N^{-1}$ is the overall Knudsen number,

$$\tilde{N}_h(\tilde{x}) = 2\pi\int_{-1}^{1}\left(\tilde{v}^2 - \frac{1}{3}\right)\tilde{h}\mathrm{d}\tilde{v}, \tag{3.4}$$

$$\tilde{M}_h(\tilde{x}) = 2\pi\int_{-1}^{1}\left(\tilde{v}^2 - \frac{3}{5}\right)\tilde{v}\tilde{h}\mathrm{d}\tilde{v}. \tag{3.5}$$

The synthetic equations are not closed because Eq. (3.3) for $\tilde{N}_h$ contains the high-order moment $\tilde{M}_h$ that is unknown in terms of lower-order moments. In this work, since we are considering phonon transport over the whole range of Knudsen numbers, we close Eqs. (3.1)-(3.3) by calculating $\tilde{M}_h$ by its definition (3.5), i.e., using the solution of the distribution function from the PBE. In this way, all the ballistic effects are included in $\tilde{M}_h$, and no truncation is introduced.

Given the distribution function $\tilde{h}^n$ and moments $\tilde{T}_h^n$, $\tilde{q}_h^n$ at the n-th iteration step, their values at the $(n+1)$-th step are updated as follows:

1. Calculate the intermediate solution of distribution function at $(n+1/2)$-th step by solving the following equation:

$$\tilde{v}\frac{\partial \tilde{h}^{n+1/2}}{\partial \tilde{x}} = \frac{\tilde{h}_{eq}^{R,n} - \tilde{h}^{n+1/2}}{Kn_R} + \frac{\tilde{h}_{eq}^{N,n} - \tilde{h}^{n+1/2}}{Kn_N} - \mathtt{i}\tilde{\omega}\tilde{h}^{n+1/2}, \tag{3.6}$$

   where the equilibrium $\tilde{h}_{eq}^{R,n}$ and $\tilde{h}_{eq}^{N,n}$ are evaluated from $\tilde{T}_h^n$, $\tilde{q}_h^n$ in Eq. (2.10), and the boundary condition is determined as per Eq. (2.12). The spatial derivative is approximated by the second-order upwind finite-difference scheme (degrades to the first-order upwind scheme at boundary).

2. Calculate the high-order moment $\tilde{M}_h^{n+1/2}$ by Eq. (3.5) and moments $\tilde{T}_h^{n+1/2}$, $\tilde{q}_h^{n+1/2}$ according to Eq. (2.11).

3. Obtain $\tilde{T}_h^{n+1}$ and $\tilde{q}_h^{n+1}$ from the macroscopic synthetic equations:

$$\frac{\partial \tilde{q}_h^{n+1}}{\partial \tilde{x}} + \mathrm{i}\tilde{\omega}\tilde{T}_h^{n+1} = 0, \tag{3.7}$$

$$\frac{1}{3}\frac{\partial \tilde{T}_h^{n+1}}{\partial \tilde{x}} + \left(\frac{1}{Kn_R} + \mathrm{i}\tilde{\omega}\right)\tilde{q}_h^{n+1} + \frac{\partial \tilde{N}_h^{n+1}}{\partial \tilde{x}} = 0, \tag{3.8}$$

$$\frac{4}{15}\frac{\partial \tilde{q}_h^{n+1}}{\partial \tilde{x}} + \left(\frac{1}{Kn_C} + \mathrm{i}\tilde{\omega}\right)\tilde{N}_h^{n+1} = -\frac{\partial \tilde{M}_h^{n+1/2}}{\partial \tilde{x}}, \tag{3.9}$$

which are closed by $\tilde{M}_h^{n+1/2}$ with boundary conditions $\tilde{T}_h^{n+1} = \tilde{T}_h^{n+1/2}$ and $\tilde{q}_h^{n+1} = \tilde{q}_h^{n+1/2}$ at boundaries.

4. Update the distribution function $\tilde{h}^{n+1} = \tilde{h}^{n+1/2}$.

The above steps are repeated until the difference between $\tilde{T}_h^n$ and $\tilde{T}_h^{n+1}$ is less than a small value. Note that if the synthetic equations are not solved, as the third step skipped, this algorithm is reduced to CIS.

3.2 Detailed implementation

Since the macroscopic synthetic equations directly seek solutions in the steady-state, attention should be paid to their numerical techniques. On substituting Eq. (3.9) into Eq. (3.8), we have

$$\frac{1}{3}\frac{\partial \tilde{T}_h^{n+1}}{\partial \tilde{x}} + \left(\frac{1}{Kn_R} + \mathrm{i}\tilde{\omega}\right)\tilde{q}_h^{n+1} - \frac{4}{15\left(\frac{1}{Kn_C} + \mathrm{i}\tilde{\omega}\right)}\frac{\partial^2 \tilde{q}_h^{n+1}}{\partial \tilde{x}^2} = \frac{1}{\frac{1}{Kn_C} + \mathrm{i}\tilde{\omega}}\frac{\partial^2 \tilde{M}_h^{n+1/2}}{\partial \tilde{x}^2}. \tag{3.10}$$

Taking the partial derivative with respect to $\tilde{x}$ on both sides of Eq. (3.7), substituting into Eq. (3.10), we obtain the following diffusion equation for $\tilde{q}_h^{n+1}$ in the $(n+1)$-th iteration step:

$$3\mathrm{i}\tilde{\omega}\left(\mathrm{i}\tilde{\omega} + \frac{1}{Kn_R}\right)\tilde{q}_h^{n+1} - \left(1 + \frac{4\mathrm{i}\tilde{\omega}}{5\left(\frac{1}{Kn_C} + \mathrm{i}\tilde{\omega}\right)}\right)\frac{\partial^2 \tilde{q}_h^{n+1}}{\partial \tilde{x}^2} = \frac{3\mathrm{i}\tilde{\omega}}{\frac{1}{Kn_C} + \mathrm{i}\tilde{\omega}}\frac{\partial^2 \tilde{M}_h^{n+1/2}}{\partial \tilde{x}^2}. \tag{3.11}$$

Similarly, taking the partial derivative with respect to $\tilde{x}$ on both sides of Eq. (3.10), combining with Eq. (3.7), we have

$$-3\mathrm{i}\tilde{\omega}\left(\mathrm{i}\tilde{\omega} + \frac{1}{Kn_R}\right)\tilde{T}_h^{n+1} + \left(1 + \frac{4\mathrm{i}\tilde{\omega}}{5\left(\frac{1}{Kn_C} + \mathrm{i}\tilde{\omega}\right)}\right)\frac{\partial^2 \tilde{T}_h^{n+1}}{\partial \tilde{x}^2} = \frac{3}{\frac{1}{Kn_C} + \mathrm{i}\tilde{\omega}}\frac{\partial^3 \tilde{M}_h^{n+1}}{\partial \tilde{x}^3}. \tag{3.12}$$

It is found that in certain regimes the eigenvalues of these second-order differential equations have large complex values, meaning that any inappropriate initial value may lead to large oscillations that decay rather slowly or even blow up. To remedy this, the small value Kn_R^{-1} in the left-hand side of Eq. (3.11) and (3.12) is replaced by a relatively large value $\bar{\delta}_R$ to decay the fast oscillation (numerical, not necessarily physical). That is, instead of solving Eq. (3.11) and (3.12), we solve the following diffuse-type equation for heat flux:

$$3\mathtt{i}\tilde{\omega}\left(\mathtt{i}\tilde{\omega}+\bar{\delta}_R\right)\tilde{q}_h^{n+1}-\left(1+\frac{4\mathtt{i}\tilde{\omega}}{5\left(\frac{1}{Kn_C}+\mathtt{i}\tilde{\omega}\right)}\right)\frac{\partial^2\tilde{q}_h^{n+1}}{\partial\tilde{x}^2}=\frac{3\mathtt{i}\tilde{\omega}}{\frac{1}{Kn_C}+\mathtt{i}\tilde{\omega}}\frac{\partial^2\tilde{M}_h^{n+1}}{\partial\tilde{x}^2}+3\mathtt{i}\tilde{\omega}\left(\bar{\delta}_R-\frac{1}{Kn_R}\right)\tilde{q}_h^{n+1/2}, \quad (3.13)$$

and temperature

$$-3\mathtt{i}\tilde{\omega}\left(\mathtt{i}\tilde{\omega}+\bar{\delta}_R\right)\tilde{T}_h^{n+1}+\left(1+\frac{4\mathtt{i}\tilde{\omega}}{5\left(\frac{1}{Kn_C}+\mathtt{i}\tilde{\omega}\right)}\right)\frac{\partial^2\tilde{T}_h^{n+1}}{\partial\tilde{x}^2}=\frac{3}{\frac{1}{Kn_C}+\mathtt{i}\tilde{\omega}}\frac{\partial^3\tilde{M}_h^{n+1}}{\partial\tilde{x}^3}-3\mathtt{i}\tilde{\omega}\left(\bar{\delta}_R-\frac{1}{Kn_R}\right)\tilde{T}_h^{n+1/2}, \quad (3.14)$$

where

$$\bar{\delta}_R=\max\left(Kn_R^{-1},\tilde{\omega}\right). \quad (3.15)$$

It can be shown that when the solutions of Eqs. (3.13) and (3.14) converge, their solutions are equivalent to Eqs. (3.11) and (3.12), respectively. This treatment does not affect the accuracy and efficiency of the GSIS, and the stability is improved.

In the diffusion regime ($Kn_R \ll 1$), the temperature profile is smooth so that the governing equation (3.14) for $\tilde{T}_h$ can be solved efficiently with the second-order central difference scheme. However, we should avoid discretising the second order derivative in the hydrodynamic regime ($Kn_N \ll 1, Kn_R \gg 1$), where the temperature profile near the boundary varies significantly [30]. To circumvent the numerical instability we consider taking the integral rather than the derivative of Eq. (3.10), and using $\tilde{T}_h^{n+1}(\tilde{x}=1/2)=\tilde{T}_h^{n+1/2}(\tilde{x}=1/2)$ as the boundary condition to calculate the temperature in the left half (the right half can be solved in a similar way):

$$\frac{\tilde{T}_h^{n+1}}{3}=\frac{\tilde{T}_h^{n+1}}{3}\bigg|_{\frac{1}{2}}^{\tilde{x}}+\frac{1}{\frac{1}{Kn_C}+\mathtt{i}\tilde{\omega}}\frac{\partial\tilde{M}_h^{n+1/2}}{\partial\tilde{x}}\bigg|_{\frac{1}{2}}^{\tilde{x}}+\frac{4}{15\left(\frac{1}{Kn_C}+\mathtt{i}\tilde{\omega}\right)}\frac{\partial\tilde{q}_h^{n+1}}{\partial\tilde{x}}\bigg|_{\frac{1}{2}}^{\tilde{x}}-\left(\frac{1}{Kn_R}+\mathtt{i}\tilde{\omega}\right)\int_{\frac{1}{2}}^{\tilde{x}}\tilde{q}_h^{n+1}\mathrm{d}\tilde{r}, \quad (3.16)$$

where $\tilde{q}_h^{n+1}$ is calculated from Eq. (3.13). The reason why we do not use $\tilde{T}_h^{n+1}(\tilde{x}=0)$ or $\tilde{T}_h^{n+1}(\tilde{x}=1)$ as boundary condition is that the boundary values from CIS are less accurate than those in the center, requiring a large number of iterations for the GSIS to capture the exact profile. Note that Eq. (3.16) cannot be a unified resolution in all transport regimes, e.g., the regimes of large values of Kn_R^{-1} would increase the integration errors in the right hand side during iteration, leading to an unstable procedure. Therefore, we use Eq. (3.14) for small Kn_R and Eq. (3.16) for large Kn_R to calculate the $\tilde{T}_h^{n+1}$ in the $(n+1)$-th iteration step. The following coefficient is introduced to make the procedure adaptable to any phonon transport regime:

$$\beta=\frac{\min(1,Kn_R)}{Kn_R}, \tag{3.17}$$

and $\tilde{T}_h^{n+1}$ is calculated by

$$\tilde{T}_h^{n+1}=\beta\tilde{T}_{h,R}^{n+1}+(1-\beta)\,\tilde{T}_{h,N}^{n+1}, \tag{3.18}$$

with $\tilde{T}_{h,R}^{n+1}$ obtained from Eq. (3.14) and $\tilde{T}_{h,N}^{n+1}$ from Eq. (3.16).

3.3 Fourier stability analysis

We employ the Fourier stability analysis to calculate the convergence rates of both CIS and GSIS in systems with periodic boundary conditions, that is, to see how fast the error decays during iteration. Firstly, we define the error function for distribution function in terms of Fourier series:

$$Y^{n+1}(\tilde{x},\tilde{v})=\tilde{h}^{n+1/2}-\tilde{h}^n=y^{n+1}(\tilde{v})\exp(\mathtt{i}\theta\tilde{x}). \tag{3.19}$$

Similarly, we define the error functions for the macroscopic quantities $\boldsymbol{M}=[\tilde{T}_h,\tilde{q}_h]^\top$ between two consecutive iteration steps as

$$\boldsymbol{\Phi}_{\boldsymbol{M}}^{n+1}(\tilde{x})=\left[\Phi_T^{n+1}(\tilde{x}),\Phi_q^{n+1}(\tilde{x})\right]^\top=\boldsymbol{M}^{n+1}(\tilde{x})-\boldsymbol{M}^n(\tilde{x})=\boldsymbol{\alpha}_{\boldsymbol{M}}^{n+1}\exp(\mathtt{i}\theta\tilde{x}), \tag{3.20}$$

where θ is the wavevector of perturbation, and $\boldsymbol{\alpha}_{\boldsymbol{M}}^{n+1}=[\alpha_T^{n+1},\alpha_q^{n+1}]^\top$ are the Fourier expansion coefficients. It is noted that we only consider the single Fourier mode $\exp(\mathtt{i}\theta\tilde{x})$ because Eq. (3.6) is linear, and all the other modes independently follow the same relation. Then, substituting Eqs. (3.19) and (3.20) into Eq. (3.6), the relation between $Y^{n+1}(\tilde{x},\tilde{v})$ and $\boldsymbol{\Phi}_{\boldsymbol{M}}^{n+1}(\tilde{x})$ can be established as

$$\tilde{v}\frac{\partial Y^{n+1}}{\partial\tilde{x}}+\left(\frac{1}{Kn_C}+\mathtt{i}\tilde{w}\right)Y^{n+1}=\frac{1}{4\pi Kn_C}\Phi_T^n+\frac{3}{4\pi Kn_N}\tilde{v}\Phi_q^n, \tag{3.21}$$

and the relation between y^{n+1} and $\boldsymbol{\alpha}_{\boldsymbol{M}}^{n+1}$ becomes

$$[1+\mathtt{i}Kn_C(\tilde{v}\theta+\tilde{w})]y^{n+1}=\frac{1}{4\pi}\alpha_T^n+\frac{3Kn_C}{4\pi Kn_N}\tilde{v}\alpha_q^n. \tag{3.22}$$

In CIS, $\boldsymbol{M}^{n+1}$ is calculated from the moments of $\tilde{h}^{n+1/2}$, so we have $\boldsymbol{\Phi}_{\boldsymbol{M}}^{n+1} = 2\pi\int_{-1}^{1} Y^{n+1}\boldsymbol{\phi}(\tilde{v})dv$, where $\boldsymbol{\phi}(v)=[1,\tilde{v}]^{\top}$. On combining Eqs. (3.19), (3.20) and (3.22), we have $\boldsymbol{\alpha}_{\boldsymbol{M}}^{n+1}=\mathbf{C}\boldsymbol{\alpha}_{\boldsymbol{M}}^{n+1}$, where the 2×2 matrix $\mathbf{C}$ is

$$\mathbf{C}=\begin{bmatrix} c_1\int_{-1}^{1} y'\mathrm{d}\tilde{v} & c_2\int_{-1}^{1}\tilde{v}y'\mathrm{d}\tilde{v} \\ c_1\int_{-1}^{1}\tilde{v}y'\mathrm{d}\tilde{v} & c_2\int_{-1}^{1}\tilde{v}^2y'\mathrm{d}\tilde{v} \end{bmatrix}, \tag{3.23}$$

with

$$c_1=\frac{1}{2},\quad c_2=\frac{3Kn_C}{2Kn_N},\quad y'=\frac{1}{1+\mathtt{i}Kn_C(\tilde{v}\theta+\tilde{w})}. \tag{3.24}$$

Clearly, the errors of macroscopic quantities propagate as $\boldsymbol{\Phi}_{\boldsymbol{M}}^{n+1}=\mathbf{C}\boldsymbol{\Phi}_{\boldsymbol{M}}^{n}=\cdots=\mathbf{C}^n\boldsymbol{\Phi}_{\boldsymbol{M}}^{1}$. Given an initial guess of the macroscopic quantities $\boldsymbol{M}^0$, we have the estimation

$$\frac{\|\boldsymbol{\Phi}_{\boldsymbol{M}}^{n+1}\|}{\|\boldsymbol{\Phi}_{\boldsymbol{M}}^{1}\|}=\frac{\|\boldsymbol{M}^{n+1}-\boldsymbol{M}^{n}\|}{\|\boldsymbol{M}^{1}-\boldsymbol{M}^{0}\|}\le\|\mathbf{C}^n\|\simeq\rho^n. \tag{3.25}$$

Here ρ is the magnitude of the largest eigenvalue of the matrix $\mathbf{C}$, i.e., the convergence rate. When $\rho>1$, the iteration is unstable; when $\rho<1$ the iteration converges, and the iteration can efficiently suppress the errors when $\rho\simeq 0$. However, the convergence is very slow when $\rho\simeq 1$.

In GSIS, $\boldsymbol{\Phi}_{\boldsymbol{M}}^{n+1}$ are not directly calculated from the integrals of the error function, but from the macroscopic synthetic equations (3.7), (3.8) and (3.9), in which $\tilde{T}_h^{n+1}$ and $\tilde{q}_h^{n+1}$ are replaced by Φ_T^{n+1} and Φ_q^{n+1}, $\tilde{N}_h^{n+1}$ is replaced by $\Phi_N^{n+1}=\tilde{N}^{n+1}-\tilde{N}^{n}=\alpha_N^{n+1}\exp(\mathtt{i}\theta\tilde{x})$, and $\tilde{M}_h^{n+1/2}$ is replaced by (because only the highest-order moment $\tilde{M}_h$ is calculated from the distribution function when solving the synthetic equations):

$$\Phi_M^{n+1/2}=\tilde{M}_h^{n+1/2}-\tilde{M}_h^{n}=2\pi\int_{-1}^{1}\left(\tilde{v}^2-\frac{3}{5}\right)\tilde{v}Y^{n+1}\mathrm{d}\tilde{v}. \tag{3.26}$$

After some simple algebras we have

$$\begin{aligned}
&\mathtt{i}\theta\alpha_q^{n+1}+\mathtt{i}\tilde{\omega}\alpha_T^{n+1}=0,\\
&\frac{1}{3}\mathtt{i}\theta\alpha_T^{n+1}+\left(\frac{1}{Kn_R}+\mathtt{i}\tilde{\omega}\right)\alpha_q^{n+1}+\mathtt{i}\theta\alpha_N^{n+1}=0,\\
&\frac{4}{15}\mathtt{i}\theta\alpha_q^{n+1}+\left(\frac{1}{Kn_C}+\mathtt{i}\tilde{\omega}\right)\alpha_N^{n+1}=-\mathtt{i}\theta 2\pi\int_{-1}^{1}\left(\tilde{v}^2-\frac{3}{5}\right)\tilde{v}y^{n+1}\mathrm{d}\tilde{v}.
\end{aligned} \tag{3.27}$$

On eliminating α_N^{n+1} and replacing y^{n+1} by its solution (3.22), we eventually obtain the 2×2 linear systems $\mathrm{L}\boldsymbol{\alpha}_{\boldsymbol{M}}^{n+1}=\mathrm{R}\boldsymbol{\alpha}_{\boldsymbol{M}}^{n}$, where

$$\begin{aligned}
\mathbf{L}&=\begin{pmatrix} \mathtt{i}\tilde{\omega} & \mathtt{i}\theta \\ \frac{1}{3}\mathtt{i}\theta & \frac{1}{Kn_R}+\mathtt{i}\tilde{\omega}+\frac{4\theta^2}{15\left(\frac{1}{Kn_C}+\mathtt{i}\tilde{\omega}\right)} \end{pmatrix},\\
\mathbf{R}&=\begin{pmatrix} 0 & 0 \\ \frac{-\theta^2c_1}{\frac{1}{Kn_C}+\mathtt{i}\tilde{\omega}}\int_{-1}^{1}\left(\tilde{v}^2-\frac{3}{5}\right)\tilde{v}y'\mathrm{d}\tilde{v} & \frac{-\theta^2c_2}{\frac{1}{Kn_C}+\mathtt{i}\tilde{\omega}}\int_{-1}^{1}\left(\tilde{v}^2-\frac{3}{5}\right)\tilde{v}^2y'\mathrm{d}\tilde{v} \end{pmatrix}.
\end{aligned} \tag{3.28}$$

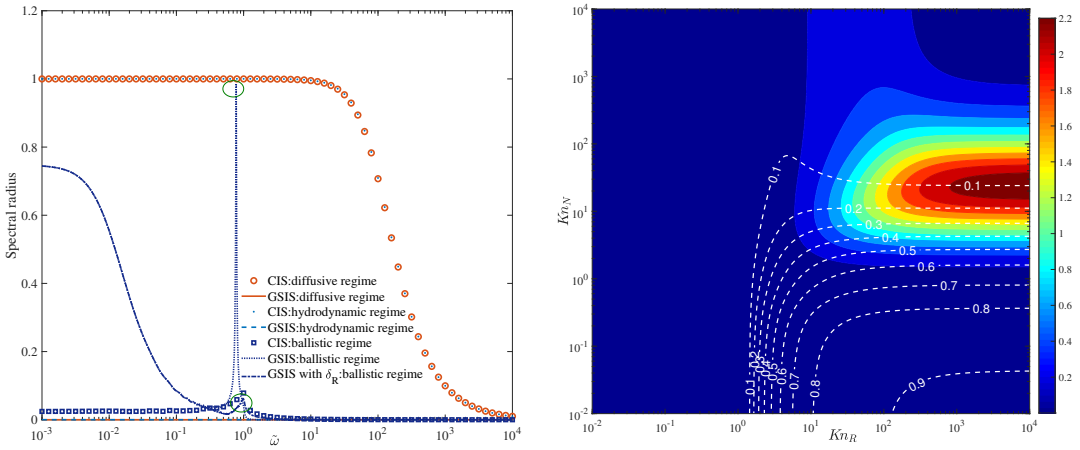

Figure 2: Left: the spectral radius ρ of CIS and GSIS versus frequency $\tilde{\omega}$ in different transport regimes, diffusive regime ($Kn_R=10^{-2}, Kn_N=10^2$), hydrodynamic regime ($Kn_R=10^2, Kn_N=10^{-2}$) and ballistic regime ($Kn_R=10^2, Kn_N=10^2$). Right: the contour of spectral radius varying with Kn_R and Kn_N at $\tilde{\omega}=0.78$, where the background is the result of original GSIS, and white dash lines are calculated from GSIS with $\bar{\delta}_R$ modified as per Eq. (3.15). The perturbation wavevector is $\theta=1$.

The convergence rates of CIS and GSIS are calculated as the spectral radius of the matrix C and $\mathrm{G}=\mathrm{L}^{-1}\mathrm{R}$, respectively. The effect of oscillation frequency in different phonon transport regimes is shown in Fig. 2. The left figure shows that the convergence of GSIS is much faster than that of CIS under small Knudsen numbers at all frequencies, which means that the error can be reduced by one order of magnitude within two iterations. However, the convergence rate of the GSIS has a sharp increase in the ballistic regime ($Kn_R \gg 1$, $Kn_N \gg 1$) in the vicinity of $\tilde{\omega}=0.7$. So, we further draw the contour of the convergence rate under different Knudsen numbers at the maximum point $\tilde{\omega}=0.78$, in the right figure. It can be seen that the convergence rate of GSIS is even larger than 1 for some combinations of Kn_R and Kn_N; that is why we introduced a parameter $\bar{\delta}_R$ in Eq. (3.15) in our algorithm to circumvent this situation. As can be seen from the white lines in Fig. 2, the convergence rate of GSIS modified with $\bar{\delta}_R$ is greatly reduced, which makes the algorithm stable in any case. While the efficiency in hydrodynamic regime is slowed down, we make a correction of $\bar{\delta}_R$ as follows, maintaining the fast convergence properties in hydrodynamic regime:

$$\bar{\delta}_R=\begin{cases}\max\left(Kn_R^{-1},\tilde{\omega}\right), & Kn_N>1,\\ Kn_R^{-1}, & Kn_N<1.\end{cases} \tag{3.29}$$

4 Fast-converging property

We compare the convergence history of temperature in both CIS and GSIS. The computational domain $\tilde{x}\in[0,1]$ is discretized by the following non-uniform grid nodes:

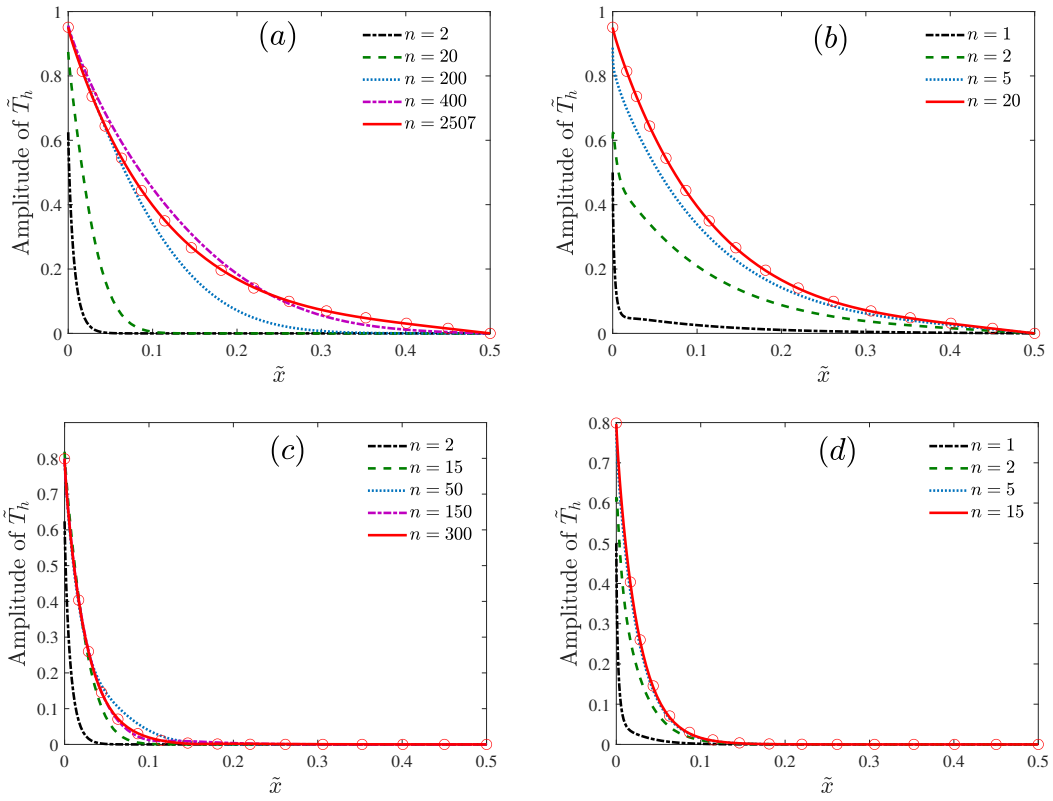

Figure 3: The amplitude of temperature at different iteration steps n in diffusion regime when $Kn_R=10^{-2}$, $Kn_N=10^2$. First row: $\tilde{\omega}=0.5$. Second row: $\tilde{\omega}=10$. Results of CIS and GSIS are shown in the left and right columns, respectively. Benchmark results (circles) are obtained from the GSIS when the iteration is converged.

$$\tilde{x}^d=d^3\left(10-15d+6d^2\right),\quad d=(0,1,\cdots,N_x-1)/(N_x-1), \tag{4.1}$$

and totally N_x=151 are used. The Gauss-Legendre quadrature with N_v=60 discrete points is adopted for the numerical integration with respect to $\tilde{v}$. We assume the iteration is converged when $\epsilon_T=\sqrt{\sum_{i=1}^{N_x}\left(\tilde{T}_{h,i}^{n+1}-\tilde{T}_{h,i}^{n}\right)^2\Delta x_i}<1\times10^{-7}$ and $\epsilon_q=\sqrt{\sum_{i=1}^{N_x}\left(\tilde{q}_{h,i}^{n+1}-\tilde{q}_{h,i}^{n}\right)^2\Delta x_i}<1\times10^{-7}$.

We first consider the heat conduction in the diffusion regime, by choosing $Kn_R=10^{-2}$ and $Kn_N=10^2$. In CIS, starting from the initial zero perturbation, Fig. 3(a) shows that the external excitation from the boundary quickly changes the temperature nearby (within about one phonon mean free path away from the boundaries). However, due to the frequent resistive scattering, it takes about 400 iteration steps for the perturbation to propagate into the bulk region. Then, it costs another 2000 steps to reach the converged profile. Such a slow convergence is completely changed in GSIS, where the temperature updated

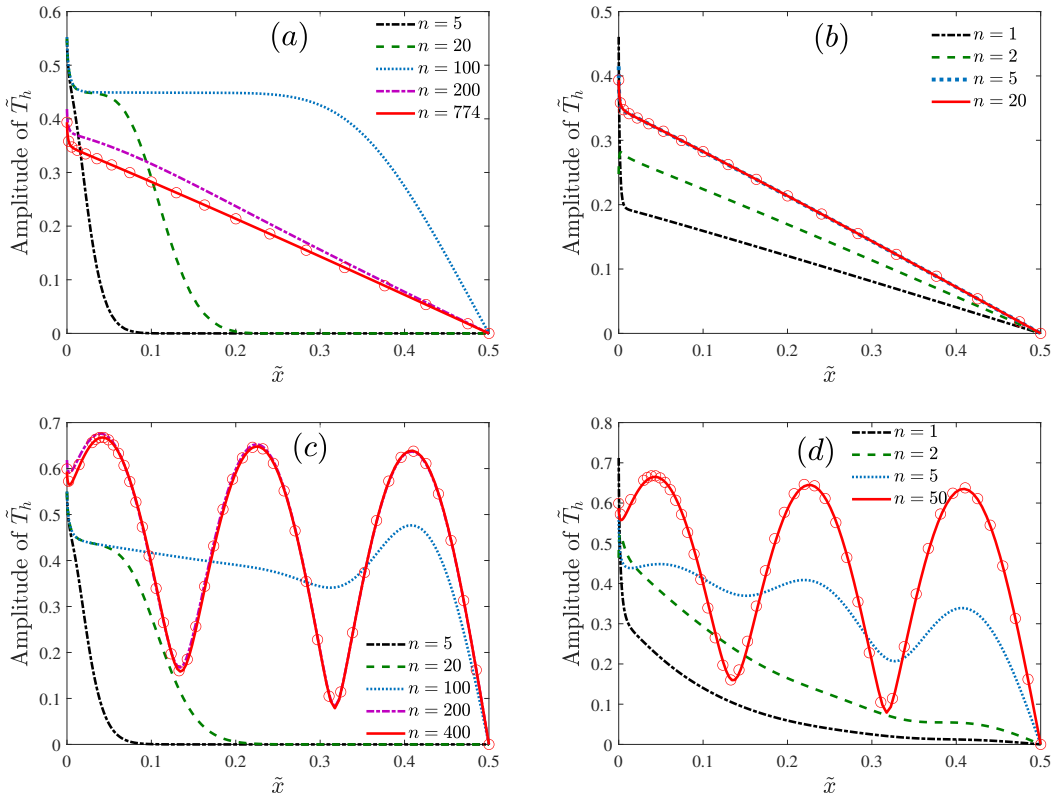

Figure 4: The amplitude of temperature at different iteration step n in hydrodynamic regime when $Kn_R=10^2$, $Kn_N=10^{-2}$. First row: $\tilde{\omega}=0.5$. Second row: $\tilde{\omega}=10$. Results of CIS and GSIS are shown in the left and right columns, respectively. Benchmark results (circles) are obtained from the GSIS when the iteration converged.

by macroscopic equations in the bulk region can be immediately corrected, leading to the fast convergence in GSIS. As seen from Fig. 3(b), the temperature in the bulk has perceived the perturbation from boundaries just after 2 iterations; and after 20 iterations the solution is converged, making the GSIS about 125 times faster than CIS. When the frequency $\tilde{\omega}$ increases, the thermal penetration depth decreases, so CIS needs fewer steps to converge. Nevertheless, GSIS is still 20 times faster.

The superiority of GSIS over CIS is also seen in the hydrodynamic regime with $Kn_R=10^2$ and $Kn_N=10^{-2}$. Due to the non-negligible effect of high-order moments, the temperature varies significantly near the boundaries. When the frequency is small ($\tilde{\omega}=0.5$), Fig. 4(a) shows that the perturbation from the boundary first propagates into the bulk region; this kind of propagation seems to have an inertia so that the temperature profile goes beyond the final converged solution after 100 steps. Then, the temperature around the left boundary decreases, which slowly regulates the temperature in the bulk region to the final state. GSIS results are illustrated in Fig. 4(b), where the slow convergence, again, is altered. It is interesting to note that the temperature is immediately

Table 1: Total iteration steps to get converged solutions under different combinations of Kn_R, Kn_N, and $\tilde{\omega}$. n_{GSIS} and n_{CIS} denote the iteration numbers of CIS and GSIS, respectively.

	diffusion regime						hydrodynamic regime					
	$Kn_R=10^{-2}, Kn_N=10^2$						$Kn_R=10^2, Kn_N=10^{-2}$					
$\tilde{\omega}$	0	0.5	1	2	10	100	0	0.5	1	2	10	100
n_{GSIS}	26	22	21	20	16	10	12	22	36	48	51	48
n_{CIS}	3106	2507	2300	2105	348	25	873	774	675	605	412	65

adjusted in the bulk region after the first iteration. When the frequency is large ($\tilde{\omega}=10$), we see in Fig. 4(c) that the temperature amplitude in bulk region is no longer a linear profile, but exhibits wave-like property; GSIS can also capture the profile within dozens of iterations.

The iteration numbers of CIS and GSIS are listed in Table 1 for other values of frequency $\tilde{\omega}$, where it can be seen that the GSIS can reduce the number of iterations up to two orders of magnitude.

5 Asymptotic-preserving property

Note that in GSIS the PBE and macroscopic synthetic equations can be solved by different numerical methods with different orders of accuracy. Now we consider the influence of spatial discretization in PBE on the accuracy of GSIS, based on the assumptions that (i) macroscopic synthetic equations can be solved exactly, and (ii) the spatial cell size Δx is able to capture the physical solution. To this end, we consider whether the Fourier diffusion equation in diffusion limit and the Guyer-Krumhansl equation in hydrodynamic limit [31] can be derived or not. $\tilde{\omega}$ is considered to be a finite number in the following analysis.

5.1 Diffusion limit ($Kn_R \to 0$, $Kn_N \to \infty$)

When the iteration is converged, the PBE (2.9) in discrete form can be written as

$$\tilde{v}\frac{\partial \tilde{h}}{\partial \tilde{x}}+\mathtt{i}\tilde{\omega}\tilde{h}+\mathcal{O}\left(\Delta x^k\right)\delta(\tilde{h})=\frac{\tilde{h}^R_{eq}-\tilde{h}}{Kn_R}, \tag{5.1}$$

where k is the order of approximation for the spatial derivative $\partial\tilde{h}/\partial\tilde{x}$, and $\delta(\tilde{h})$ is the $(k+1)$-th order derivative of $\tilde{h}$. For instance, when the second-order upwind finite-difference scheme is used, we have $k=2$.

In the Chapman-Enskog expansion [32], the distribution function is approximated by the Taylor expansion: $\tilde{h}=h_0^R+Kn_R h_1^R+\mathcal{O}\left(Kn_R^2\right)$. Substituting this expansion into Eq. (5.1) and collecting terms with the order of Kn_R^{-1}, we have $h_0^R=\tilde{h}^R_{eq}$. When the following largest

scaling is chosen:

$$\Delta x \sim Kn_R^{1/\infty} = \mathcal{O}(1), \tag{5.2}$$

by collecting terms with the order Kn_R^0, we have $h_1^R = -\tilde{v}\frac{\partial \tilde{h}_{eq}^R}{\partial \tilde{x}} - \mathtt{i}\tilde{\omega}\tilde{h}_{eq}^R - \delta\left(\tilde{h}_{eq}^R\right)$. According to the definition of $\tilde{M}_h$ in Eq. (3.5), we obtain the higher-order moment

$$\begin{aligned}\tilde{M}_h &= 2\pi\int_{-1}^{1}\left(\tilde{v}^2-\frac{3}{5}\right)\tilde{v}\left[\frac{\tilde{T}_h}{4\pi}-\frac{Kn_R}{4\pi}\frac{\partial\tilde{T}_h}{\partial\tilde{x}}\tilde{v}-Kn_R\mathtt{i}\tilde{\omega}\frac{\tilde{T}_h}{4\pi}-Kn_R\delta\left(\tilde{h}_{eq}^R\right)+\mathcal{O}\left(Kn_R^2\right)\right]\mathrm{d}\tilde{v}\\ &= \mathcal{O}\left(Kn_R^2\right).\end{aligned}$$

Therefore, with Eqs. (3.1), (3.2) and (3.3), we obtain the governing equation for the temperature $\tilde{T}_h$ and heat flux $\tilde{q}_h$:

$$\begin{aligned}&\left(\frac{Kn_R}{3}+\frac{4\mathtt{i}\tilde{\omega}Kn_R^2}{15}\right)\frac{\partial^2\tilde{T}_h}{\partial\tilde{x}^2} = \mathtt{i}\tilde{\omega}\left(1+\mathtt{i}\tilde{\omega}Kn_R\right)\tilde{T}_h,\\ &\tilde{q}_h = -\left(\frac{Kn_R}{3}+\frac{4\mathtt{i}\tilde{\omega}Kn_R^2}{15}\right)\frac{\partial\tilde{T}_h}{\partial\tilde{x}}.\end{aligned} \tag{5.3}$$

Especially in the limit of $\tilde{\omega}=0$, Eq. (5.3) is reduced to the well-known Fourier heat conduction equation, with the second-order accuracy of Knudsen number:

$$\nabla^2\tilde{T}_h+\mathcal{O}\left(Kn_R^2\right)=0, \quad \tilde{q}_h = -\frac{Kn_R}{3}\frac{\partial\tilde{T}_h}{\partial\tilde{x}}+\mathcal{O}\left(Kn_R^2\right). \tag{5.4}$$

Similarly, we find that the Fourier heat conduction law can be recovered in CIS, with the second-order of accuracy of Knudsen number, when

$$\Delta x = \mathcal{O}(Kn_R^{1/k}). \tag{5.5}$$

Therefore, as long as the spatial resolution $\Delta x=\mathcal{O}(1)$ is able to capture the physical solution, GSIS recovers Fourier's law of heat conduction when $Kn_R\to 0$. However, CIS needs more spatial grids when comparing Eqs. (5.2) with (5.5). This property can be observed in our numerical results in Fig. 5: GSIS accurately captures the solution with only 20 grid cells, while CIS requires 3 times more grids than GSIS. The higher the frequency, the faster the amplitude of temperature decays and the more grids CIS needs.

5.2 Hydrodynamic limit ($Kn_R\to\infty$, $Kn_N\to 0$)

Similarly, the PBE (2.9) in discrete form can be written as

$$\tilde{v}\frac{\partial\tilde{h}}{\partial\tilde{x}}+\mathtt{i}\tilde{\omega}\tilde{h}+\mathcal{O}\left(\Delta x^k\right)\delta(\tilde{h}) = \frac{\tilde{h}_{eq}^N-\tilde{h}}{Kn_N}. \tag{5.6}$$

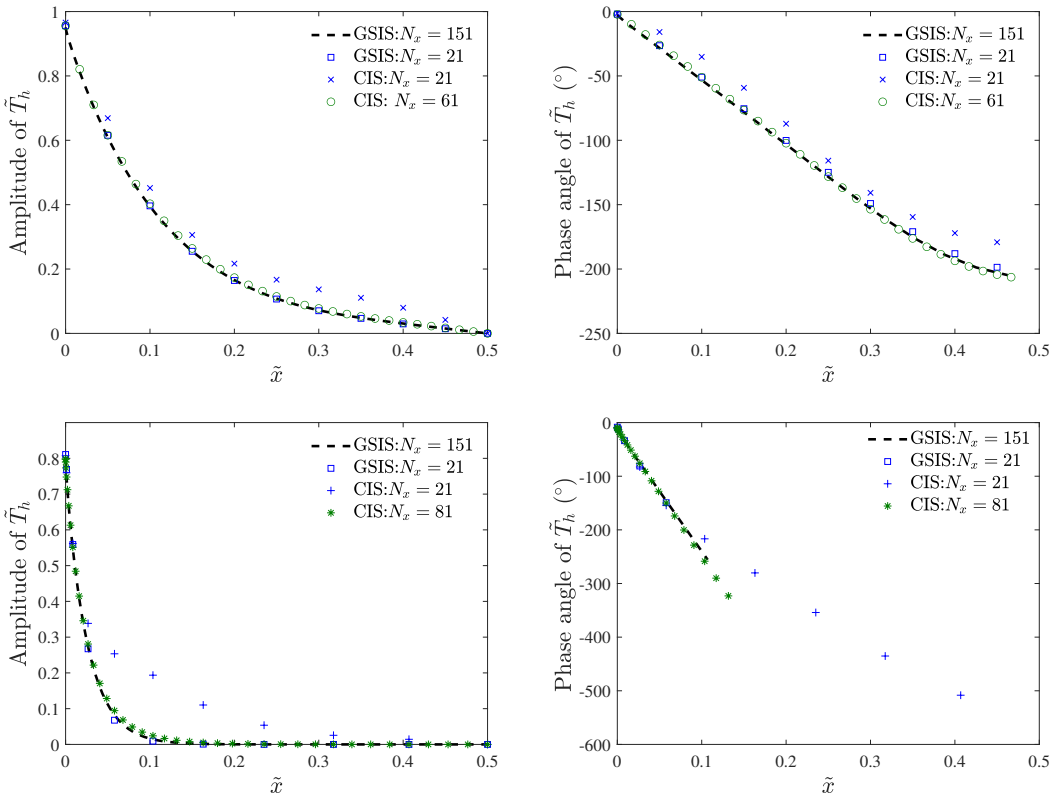

Figure 5: Asymptotic-preserving property in the diffusion regime ($Kn_R = 10^{-2}$, $Kn_N = 10^2$). The amplitude and phase angle of temperature $\tilde{T}_h$ with oscillation frequency (top) $\tilde{\omega} = 0.5$ and (bottom) $\tilde{\omega} = 10$. In GSIS, macroscopic synthetic equations are solved by the second-order central difference scheme.

Expressing the distribution function as $\tilde{h} = h_0^N + Kn_N h_1^N + \mathcal{O}(Kn_N^2)$, and collecting the order of Kn_N^{-1} and Kn_N^0, respectively, we have $h_0^N = \tilde{h}_{eq}^N$ and $h_1^N = -\tilde{v}\frac{\partial \tilde{h}_{eq}^N}{\partial \tilde{x}} - \mathrm{i}\tilde{\omega}\tilde{h}_{eq}^N - \delta(\tilde{h}_{eq}^N)$ when the following scale is chosen:

$$\Delta x \sim Kn_N^{1/\infty} = \mathcal{O}(1). \tag{5.7}$$

In this case, with Eq. (3.5), we obtain

$$\begin{aligned}\tilde{M}_h =& 2\pi \int_{-1}^{1} \left(\tilde{v}^2 - \frac{3}{5}\right)\tilde{v}\left[\frac{\tilde{T}_h}{4\pi} + \frac{3\tilde{q}_h\tilde{v}}{4\pi} - \frac{Kn_N}{4\pi}\frac{\partial \tilde{T}_h}{\partial \tilde{x}}\tilde{v} - \frac{3Kn_N}{4\pi}\frac{\partial \tilde{q}_h}{\partial \tilde{x}}\tilde{v}^2\right.\\ &\left. - Kn_N \mathrm{i}\tilde{\omega}\frac{\tilde{T}_h}{4\pi} - Kn_N \mathrm{i}\tilde{\omega}\frac{3\tilde{q}_h}{4\pi}\tilde{v} - Kn_N\delta\left(\tilde{h}_{eq}^N\right) + \mathcal{O}\left(Kn_N^2\right)\right]\mathrm{d}\tilde{v}\\ =& \mathcal{O}\left(Kn_N^2\right).\end{aligned}$$

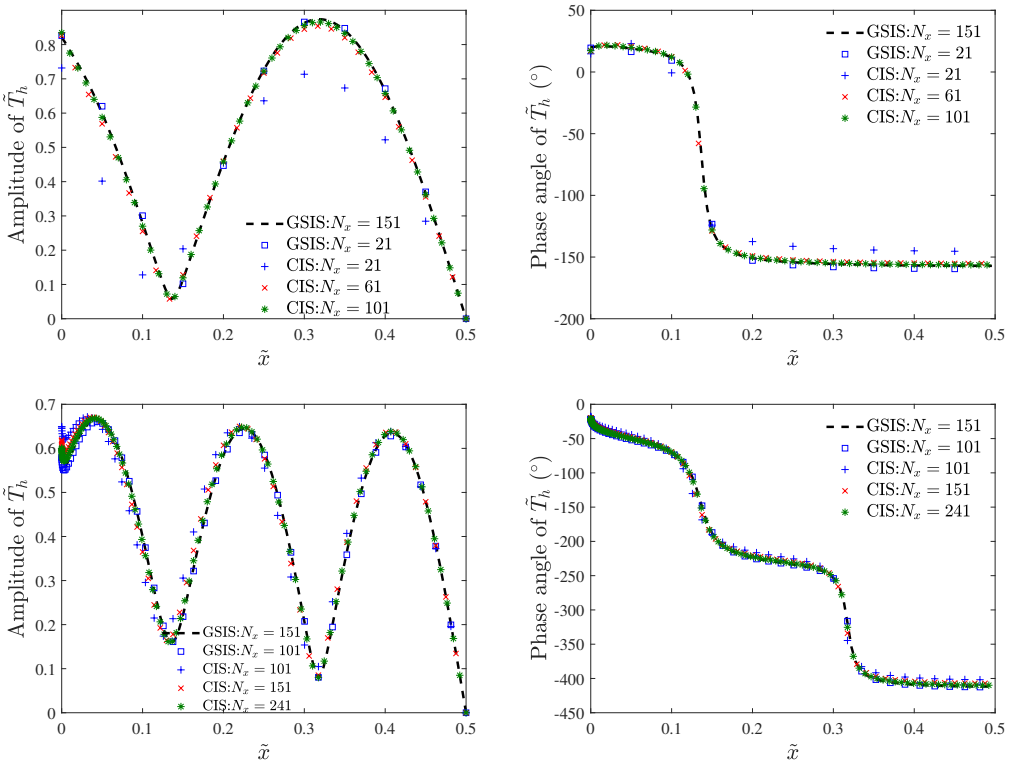

Figure 6: Asymptotic-preserving property in the hydrodynamic regime ($Kn_R = 10^2, Kn_N = 10^{-2}$). The amplitude and phase angle of temperature $\tilde{T}_h$ with oscillation frequency (top) $\tilde{\omega} = 5$ and (bottom) $\tilde{\omega} = 10$. In GSIS, macroscopic synthetic equations are solved by the second-order central difference scheme.

Combining Eqs. (3.1), (3.2) and (3.3), we obtain

$$\begin{aligned} &\frac{\partial \tilde{q}_h}{\partial x} + \mathrm{i}\omega \tilde{T}_h = 0, \\ &\frac{1}{3}\frac{\partial \tilde{T}_h}{\partial \tilde{x}} + \left(\frac{1}{Kn_R} + \mathrm{i}\tilde{\omega}\right)\tilde{q}_h - \frac{4}{15\left(\frac{1}{Kn_C} + \mathrm{i}\tilde{\omega}\right)}\frac{\partial^2 \tilde{q}_h}{\partial \tilde{x}^2} = 0 + \mathcal{O}\left(Kn_N^2\right). \end{aligned} \tag{5.8}$$

Thus, in the special case of $\tilde{\omega} = 0$, we obtain a system very similar to the well-known Guyer-Krumhansl equations for phonon hydrodynamics. In contrast, in CIS the Guyer-Krumhansl equations can be recovered with the second-order accuracy of Knudsen number, when the following largest scale is used:

$$\Delta x = \mathcal{O}(Kn_N^{1/k}). \tag{5.9}$$

Thus, GSIS recovers the Guyer-Krumhansl equation when $Kn_N \to 0$ even with coarse spatial grids $\Delta x = \mathcal{O}(1)$. Therefore, the overall order of accuracy of GSIS depends only on the order of solving macroscopic synthetic equations. As shown in Fig. 6, when $\tilde{\omega} = 5$,

$N_x=21$ is adequate for GSIS to get the accurate solution, while CIS requires $N_x=101$. When $\tilde{\omega}=10$, the frequency of temperature amplitude becomes higher, and GSIS needs $N_x=101$ grids to capture the dynamical properties. The CIS, however, needs more than $N_x=241$ grids if we pay attention to the (not so converged) temperature profile at the left boundary.

6 Heat conduction in different regimes

With the accurate and efficient numerical method, now we are in the position to investigate the non-equilibrium heat conduction in different flow regimes, spanning the whole region of oscillation frequency $\tilde{\omega}$.

6.1 Bounded length case

Consider the bounded domain as shown in Fig. 1. In the diffusion regime ($Kn_R=10^{-2}$, $Kn_N=10^2$), as can be seen in Fig. 7, with $\tilde{\omega}$ increasing, the temperature near the boundary changes more and more dramatically, and the intermediate area where the temperature is not affected becomes larger and larger. When $\tilde{\omega}=0$, the heat flux is a constant within the whole domain; as the frequency becomes higher, the boundary heat flux increases, while the central heat flux decreases to zero, i.e., the thermal penetration depth gets smaller. This is because if the boundary temperature oscillates too fast, there is not enough time for phonons in central bulk region to follow the variation. In all the frequencies considered, the phases of temperature and heat flux are nearly linear functions of $\tilde{x}$ when $\tilde{x}$ is small, where the slopes increase significantly with the oscillation frequency $\tilde{\omega}$.

Fig. 8 shows that the frequency effect in the hydrodynamic regime ($Kn_R=10^2$, $Kn_N=10^{-2}$) is different to the diffusion regime. When $\tilde{\omega}=0$, the temperature in the bulk region remains close to zero, with only an extremely narrow region near the boundary showing a rapid variation. As $\tilde{\omega}$ increases, the central temperature is increased, which keeps a near-linear profile; the heat flux changes from a constant to a concave distribution of $\tilde{x}$, with the maximum value appearing at the central position $\tilde{x}=1/2$. On the other hand, when $\tilde{\omega}$, the phases of temperature and heat flux are near constants in the bulk regime. It is interesting to note that the heat conduction is quite complicated as $\tilde{\omega}$ further increases. As we can see in the bottom two rows of Fig. 8, the amplitudes of temperature and heat flux do not exhibit monotonous distributions, but wave-like distributions. When $\tilde{\omega}$ is huge, the phenomena are similar to those in the diffusion regime. This similarity pushes us to seek the analytical solution at high frequency limit. When $\tilde{\omega}Kn_R$, $\tilde{\omega}Kn_N$, and $\tilde{\omega}$ approach infinity, the resistive and normal scatterings can be ignored, and the PBE is rewritten as $\tilde{v}\partial\tilde{h}/\partial\tilde{x}+\mathrm{i}\tilde{\omega}\tilde{h}=0$, the solution of which is $\tilde{h}=C\exp\left(-\frac{\mathrm{i}\tilde{\omega}}{\tilde{v}}\tilde{x}\right)$. When $\tilde{v}<0$, we

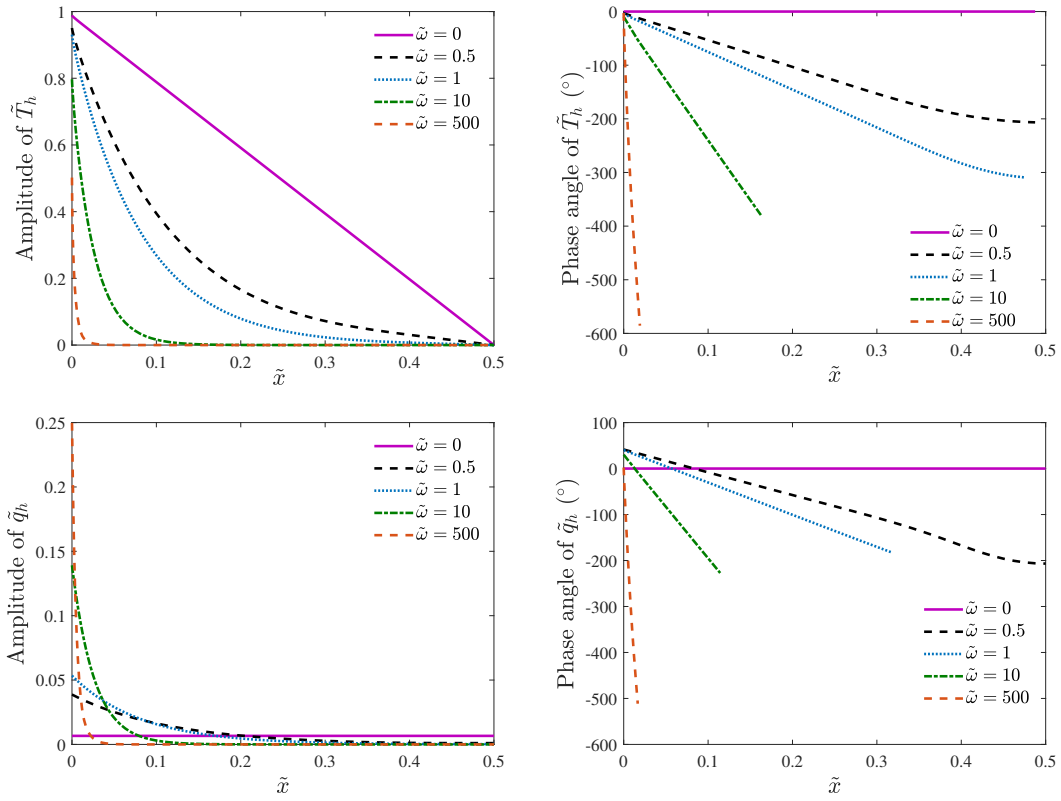

Figure 7: The amplitude and phase angle of temperature $\tilde{T}_h$ and heat flux $\tilde{q}_h$ distribution with different oscillation frequency $\tilde{\omega}$ in diffusion regime ($Kn_R=10^{-2}, Kn_N=10^2$).

have $C=0$; when $\tilde{v}>0$, the left boundary gives $C=\tilde{h}(\tilde{v}>0,\tilde{x})=1/4\pi$. Therefore,

$$\tilde{T}_h=2\pi\int_{0^+}^{1}C(\tilde{v})\exp\left(-\frac{\mathrm{i}\tilde{\omega}}{\tilde{v}}\tilde{x}\right)\mathrm{d}\tilde{v}=\begin{cases}\frac{1}{2}, & \tilde{x}=0,\\ 0, & \text{otherwise},\end{cases} \tag{6.1}$$

$$\tilde{q}_h=2\pi\int_{0^+}^{1}C(\tilde{v})\tilde{v}\exp\left(-\frac{\mathrm{i}\tilde{\omega}}{\tilde{v}}\tilde{x}\right)\mathrm{d}\tilde{v}=\begin{cases}\frac{1}{4}, & \tilde{x}=0,\\ 0, & \text{otherwise},\end{cases} \tag{6.2}$$

which is consistent with our numerical results shown in Figs. 7 and 8, where the left wall temperature and heat flux approach 0.5 and 0.25, respectively. Note that the high frequency limit is different to the common ballistic regime ($Kn_R\to\infty, Kn_N\to\infty, \tilde{\omega}\to 0$), where the PBE is reduced to $\tilde{v}\partial\tilde{h}/\partial\tilde{x}=0$, with the solution $\tilde{h}(\tilde{v}>0,\tilde{x})=1/4\pi$ and $\tilde{h}(\tilde{v}<0,\tilde{x})=-1/4\pi$. Therefore, the temperature is $\tilde{T}_h(\tilde{x})=2\pi\int_{-1}^{0}\tilde{h}\mathrm{d}\tilde{v}+2\pi\int_{0}^{1}\tilde{h}\mathrm{d}\tilde{v}=0$, and the heat flux is $\tilde{q}_h(\tilde{x})=1/2$.

We now quantitatively investigate the frequency effect on thermal conduction, by plotting the surface temperature and heat flux over a wide range of $\tilde{\omega}$ in Fig. 9. In the

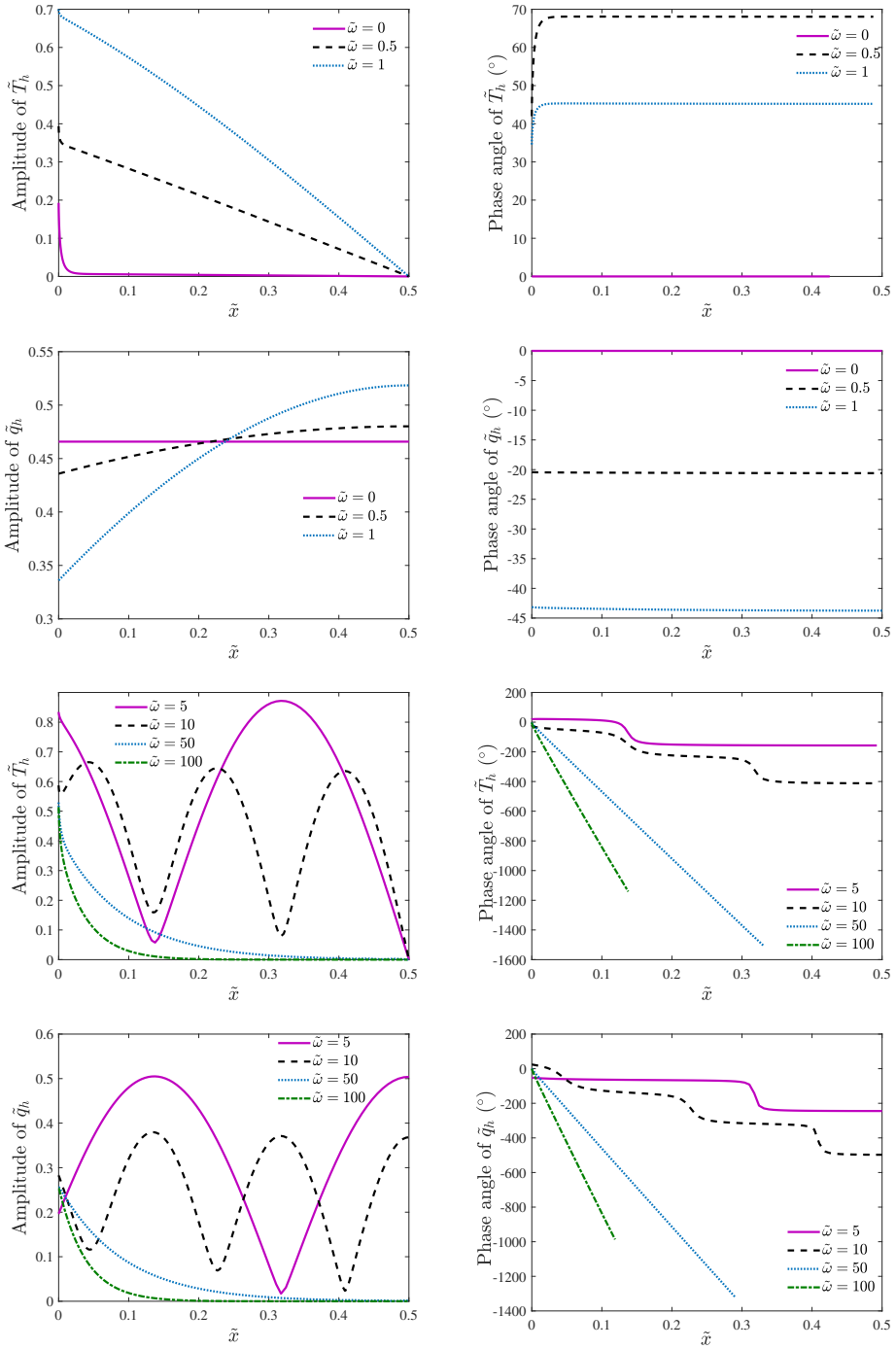

Figure 8: The amplitude and phase angle of temperature $\tilde{T}_h$ and heat flux $\tilde{q}_h$ distribution for different oscillation frequency $\tilde{\omega}$ in hydrodynamic regime ($Kn_R=10^2, Kn_N=10^{-2}$).

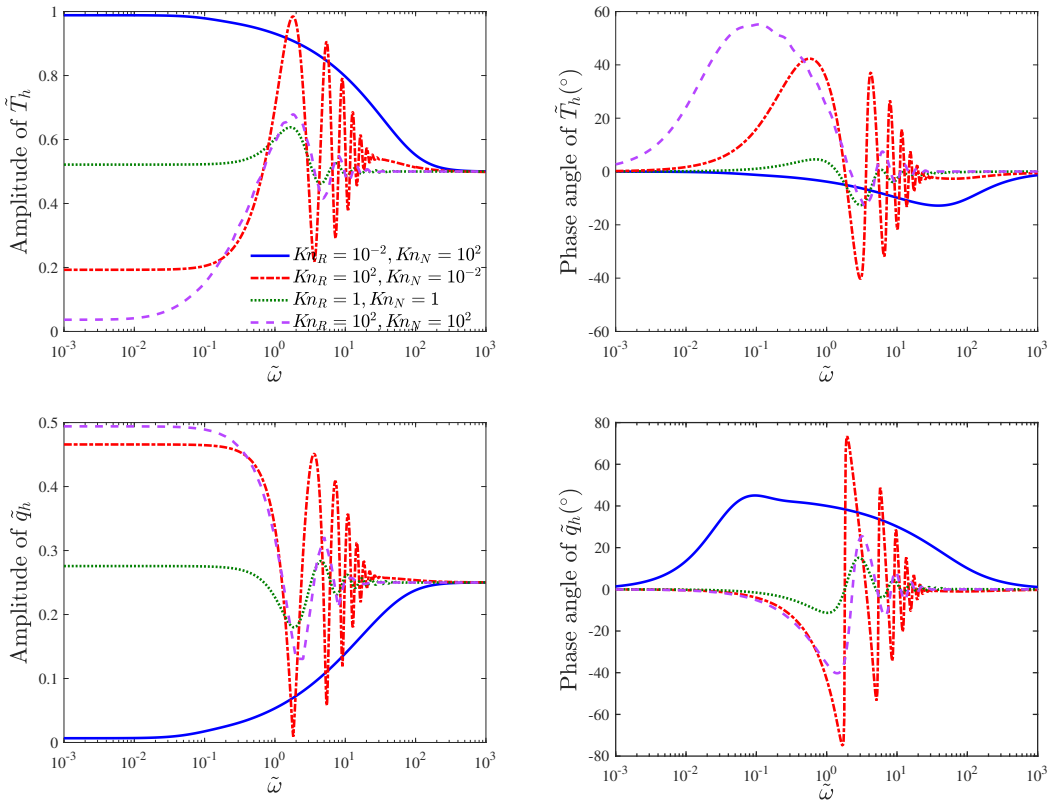

Figure 9: The amplitude and phase angle of temperature $\tilde{T}_h$ and heat flux $\tilde{q}_h$ at left boundary $\tilde{x}=0$ versus the oscillation frequency $\tilde{\omega}$ in different phonon transport regimes.

diffusive regime ($Kn_R = 10^{-2}$, $Kn_N = 10^2$), the surface temperature varies synchronously with the heating wall at low frequency limit, so we can easily determine that the temperature amplitude is 1 and the temperature phase angle is 0. Since Eq. (5.3) can be reduced to Eq. (5.4) at low frequency limit even without $\tilde{\omega}=0$ (since $\tilde{\omega}$ is a higher order infinitesimal of Kn_R in the bounded length case), the heat flux can be determined by $\tilde{q}_h = -\frac{Kn_R}{3}\frac{\partial T}{\partial x} = 0.0067$, and the phase angle remains zero. On the contrary, when the frequency goes to infinity, the analytical solutions that the surface temperature and heat flux approach $1/2$ and $1/4$, regardless of the values of Kn_R and Kn_N, is in good agreement with our numerical results. In the intermediate region of $\tilde{\omega}$, the amplitudes of temperature and heat flux amplitude vary monotonically from the low frequency limit to the high frequency limit, in the diffusion regime. While if the resistive scattering gets weaker (Kn_R increases), the surface temperature amplitude decreases and the surface heat flux amplitude increases. Furthermore, the properties versus frequency are much more complicated for a transient regime of $\tilde{\omega} \in \left[10^{-1}, 10^{1}\right]$, where the curve oscillates violently: the larger the Kn_R, the stronger the oscillation.

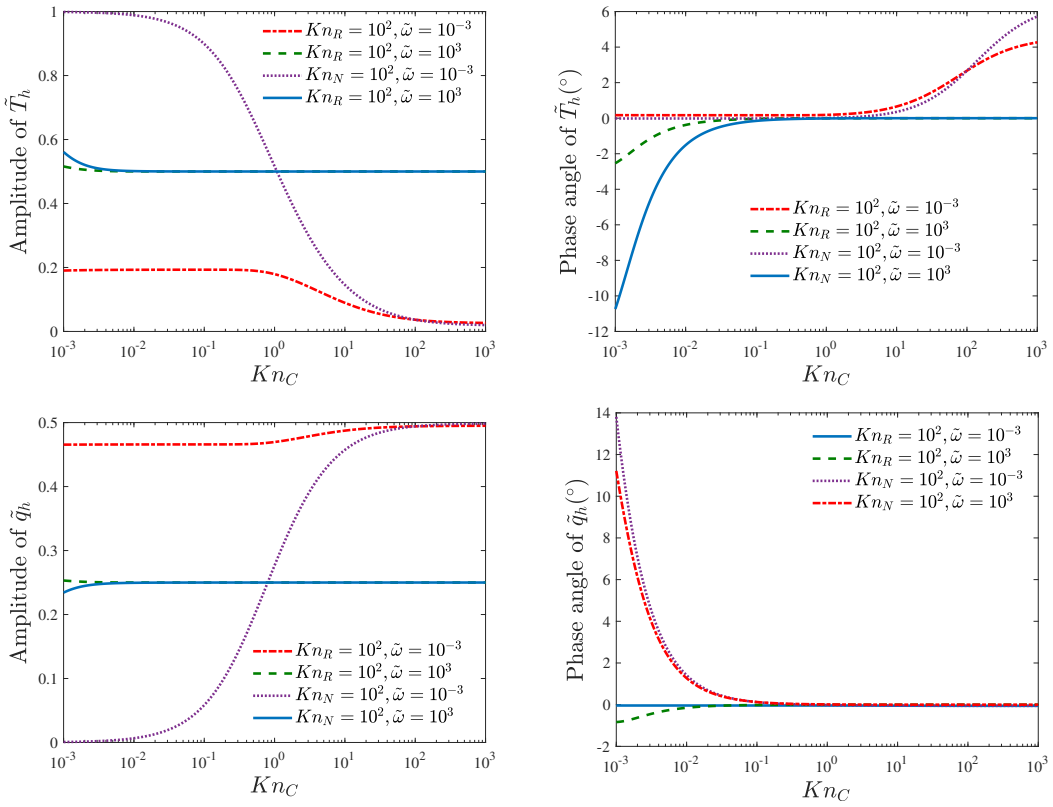

Figure 10: The amplitude and phase angle of temperature $\tilde{T}_h$ and heat flux $\tilde{q}_h$ at left boundary $\tilde{x}=0$ versus the overall Knudsen number Kn_C in different phonon transport regimes at low and high frequency limit.

We have mentioned above that the decrease of Kn_R leads to the decrease of surface temperature amplitude, a more detailed study of how much the two Knudsen numbers influence these thermal properties is necessary. Thus, we fix one Knudsen number, and observe how another Knudsen number affects the amplitude and phase angle of $\tilde{T}_h$ and $\tilde{q}_h$ at low frequency limit ($\tilde{\omega}=10^{-3}$) and high frequency limit ($\tilde{\omega}=10^3$), respectively. From Fig. 10, it is found that either Kn_R or Kn_N leads to a decrease in the surface temperature amplitude and an increase in the surface heat flux amplitude, and Kn_R has a greater effect on both temperature and heat flux than Kn_N at both high and low frequency limits. In addition, the Knudsen effect is quiescent at high frequency limit, remaining almost constant with Kn_N varying, which implies that the normal scattering requires a lower heating frequency to reach the high frequency limit resolution than the resistive scattering.

6.2 Semi-infinite length case

Here we concentrate on the heat conduction in a semi-infinite solid, as most existing studies do, except that the normal scattering is also taken into account. It is clear that

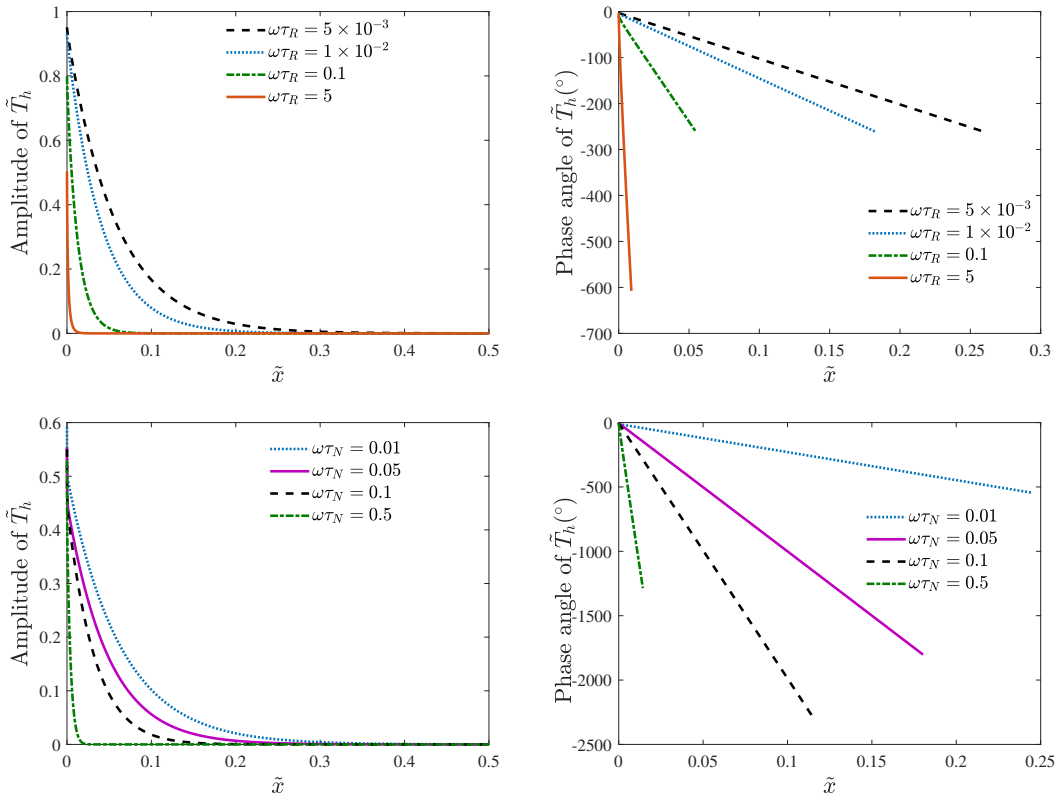

Figure 11: The amplitude and phase angle of temperature $\tilde{T}_h$ for different oscillation frequency in semi-infinite length case with (top) $\tau_R = 10^{-2}$, $\tau_N = 10^2$ and (bottom) $\tau_R = 10^2$, $\tau_N = 10^{-2}$.

the length of simulation domain L cannot be infinite, so we keep trying to increase L so that the temperature amplitude decays to zero, i.e., the value of L no longer affects the profiles of temperature and heat flux. Considering only resistive scattering or only normal scattering, we know that this problem is determined by the dimensionless parameter $\hat{\omega} = \omega\tau$ (τ can be τ_R or τ_N) through dimension analysis, so we fix one relaxation time to be infinitely large (10^2), and another relaxation time to be small (10^{-2}), and simulate the problem under different values of frequencies. We introduce two quantities that are commonly measured in experiments: the thermal penetration depth L_p, defined as the depth at which the temperature amplitude decays to 0.01, normalized by the phonon mean free path $|v|\tau$; and the phase lag between the surface temperature and heat flux:

$$\Psi = \mathrm{Arg}[\tilde{q}_h(\tilde{x}=0)] - \mathrm{Arg}[\tilde{T}_h(\tilde{x}=0)], \tag{6.3}$$

where Arg denotes taking the phase angle of a complex number.

To compare the two simulated cases, we first plot the temperature amplitude profiles at different selected frequencies in Fig. 11, with ω and τ identical to those in the bounded

length case. The variation with frequency is similar to the previous case in the diffusion regime, but neither the amplitude nor the phase angle of $\tilde{T}_h$ and $\tilde{q}_h$ shows the complicated wave-like property in the hydrodynamic regime. Having built the general idea that there exists difference in two cases, we continue to investigate the surface thermal properties varying with frequency in order to quantitatively distinguish the semi-infinite case from the bounded-length case, shown in Fig. 12. From Fig. 12(a-d), we see that the temperature and heat flux at high frequency are consistent with our theoretical derivation in the bounded case. This is because the thermal penetration depth is quite small at high frequencies, so this case does not differ from the bounded case. However, the properties at low frequencies are different from those in bounded case, because low frequencies require larger length for the temperature amplitude to decay to zero, so the choice of length is significant for the simulation. It is interesting to find that the thermal penetration depth follows a linear relationship with frequency in the diffusion regime from Fig. 12(e); for small frequencies, L_p in hydrodynamic regime is much larger than that in diffusion regime, and the two lengths get closer and closer as $\hat{\omega}$ increases. Such a quantitative description of L_P gives us an efficient guide for choosing L ($L > L_P$). When $\hat{\omega} \to 0$, the phase lag approaches $\pi/4$ if there is only resistive scattering, as shown in Fig. 12(f). Related to the dimensionless parameters introduced in Eq. (2.4), since L is infinite, we have $Kn_R \to 0$ and $\tilde{\omega} \to 0$ for small ω. Recalling Eq. (5.3), since $\tilde{\omega}$ is an infinitesimal of the same order as Kn_R, the conduction equation cannot be reduced to Eq. (5.4). Keeping the first-order minima of Kn_R and $\tilde{\omega}$, we have the governing equation,

$$\frac{Kn_R}{3}\frac{\mathrm{d}^2\tilde{T}_h}{\mathrm{d}\tilde{x}^2} - \mathtt{i}\tilde{\omega}\tilde{T}_h = 0. \tag{6.4}$$

Since the length is infinite, the temperature cannot grow exponentially with x, the real part of the eigenvalue should be positive. So the general solution of Eq. (6.4) is

$$\tilde{T}_h = C\exp(\lambda\tilde{x}), \quad \lambda = \sqrt{\frac{3\tilde{\omega}}{Kn_R}}\exp\left(\mathtt{i}\frac{5\pi}{4}\right). \tag{6.5}$$

The heat flux can be determined by the Fourier law,

$$\tilde{q} = -\frac{Kn_R}{3}\frac{\partial\tilde{T}}{\partial\tilde{x}} = -\frac{Kn_R}{3}\exp(\mathtt{i}\tilde{\omega}\tilde{t})C\lambda\exp(\lambda\tilde{x}), \tag{6.6}$$

so the phase lag defined in Eq. (6.3) can be calculated by

$$\begin{aligned}\Psi &= \mathrm{Arg}\left[\frac{\tilde{q}(\tilde{x})}{\tilde{T}(\tilde{x})}\right] = \mathrm{Arg}\left[\frac{\tilde{q}_h(\tilde{x})}{\tilde{T}_h(\tilde{x})}\right] \\ &= \mathrm{Arg}\left[-\frac{\frac{Kn_R}{3}C\lambda\exp(\lambda\tilde{x})}{C\exp(\lambda\tilde{x})}\right] = \mathrm{Arg}\left[-\frac{Kn_R}{3}\lambda\right] = \frac{\pi}{4}.\end{aligned} \tag{6.7}$$

Note that with above derivation, the conclusion that the phase lag in Fourier limit is $\pi/4$ is valid not only at the surface $\tilde{x} = 0$, but also at any spatial position.

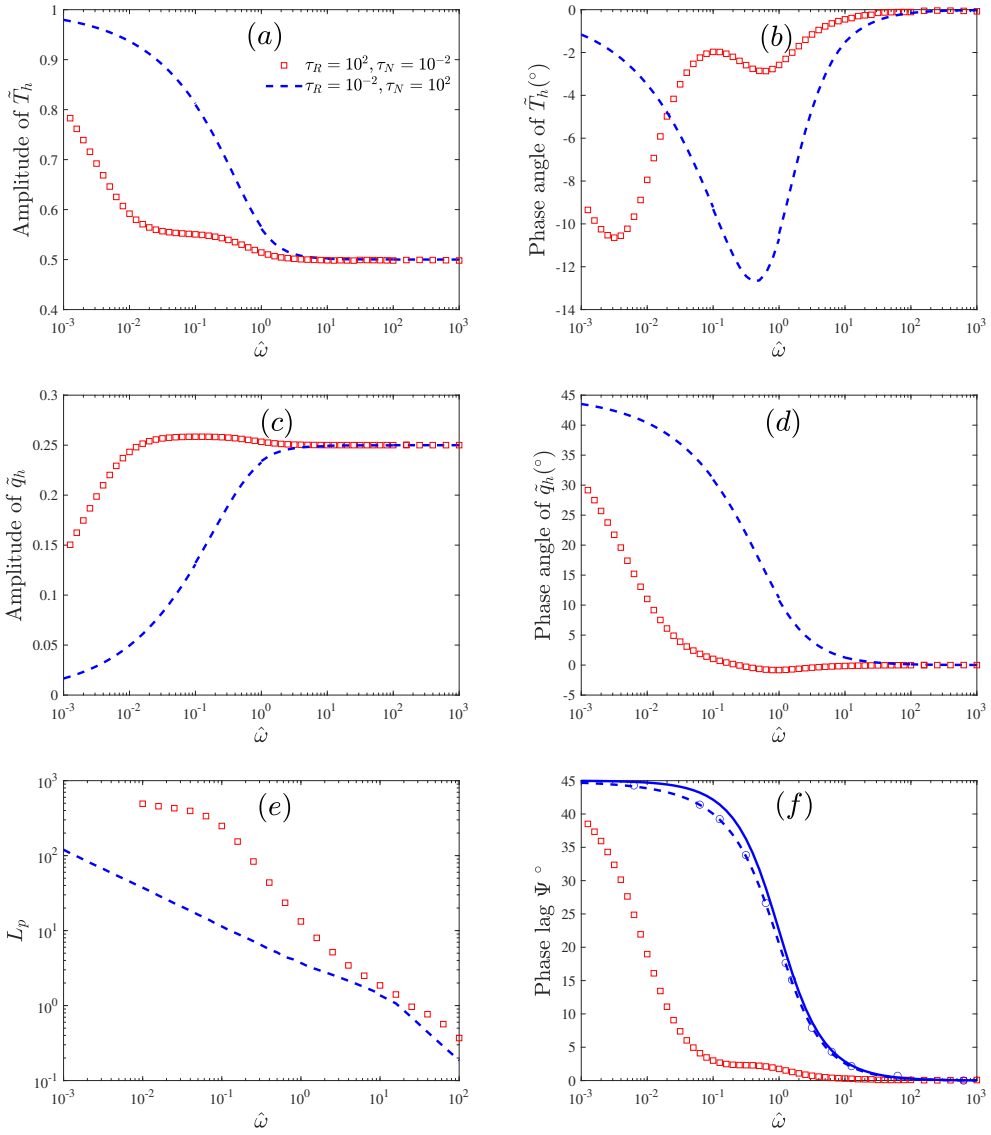

Figure 12: The amplitude and phase angle of temperature $\tilde{T}_h$ and heat flux $\tilde{q}_h$, and phase lag Ψ at the left boundary $\tilde{x}=0$, and the thermal penetration L_p versus the oscillation frequency $\hat{\omega}$ in different phonon transport regimes, where dotted lines and squares calculated from our scheme GSIS, solid line from Yang et al. [33], circles from Huberman et al. [34].

7 Conclusions

We have extended the GSIS to speed up the convergence of the conventional iterative scheme in solving frequency domain thermoreflectance problem based on phonon Boltzmann equation. The Fourier stability analysis has been performed to rigorously prove

that the GSIS can rapidly converge for a wide range of Knudsen numbers and frequencies. Additionally, we have proven that the GSIS asymptotically preserves the Fourier law in diffusive limit and Guyer-Krumhansl equations in hydrodynamic limit in coarse spatial grids: in the bulk region the spatial cell size can be $\Delta x \sim \mathcal{O}(1)$, as long as this size is adequate for capturing the dynamical properties. However, finer grids are required to capture the exact structures for high frequencies, as the temperature amplitude near the surface decreases significantly with increasing heating frequency $\tilde{\omega}$. This is a disaster for conventional explicit time-marching kinetic solvers, but poses no problems for GSIS. One reason for this is that GSIS is an implicit solver, and the other is that the time variable is removed by Fourier expansion. In this way, we can avoid great computational consumption brought from small temporal grids through adopting non-uniform spatial grid.

References

[1] G. Chen, Non-Fourier phonon heat conduction at the microscale and nanoscale, Nat. Rev. Phys. 3 (8) (2021) 555–569.

[2] D. G. Cahill, P. V. Braun, G. Chen, D. R. Clarke, S. Fan, K. E. Goodson, P. Keblinski, W. P. King, G. D. Mahan, A. Majumdar, et al., Nanoscale thermal transport. II. 2003–2012, Appl. Phys. Rev. 1 (1) (2014) 011305.

[3] I. Chowdhury, R. Prasher, K. Lofgreen, G. Chrysler, S. Narasimhan, R. Mahajan, D. Koester, R. Alley, R. Venkatasubramanian, On-chip cooling by superlattice-based thin-film thermoelectrics, Nat. Nanotechnol. 4 (4) (2009) 235–238.

[4] A. I. Hochbaum, R. Chen, R. D. Delgado, W. Liang, E. C. Garnett, M. Najarian, A. Majumdar, P. Yang, Enhanced thermoelectric performance of rough silicon nanowires, Nature 451 (7175) (2008) 163–167.

[5] K. Hamad-Schifferli, J. J. Schwartz, A. T. Santos, S. Zhang, J. M. Jacobson, Remote electronic control of dna hybridization through inductive coupling to an attached metal nanocrystal antenna, Nature 415 (6868) (2002) 152–155.

[6] S. G. Volz, Thermal insulating behavior in crystals at high frequencies, Phys. Rev. Lett. 87 (2001) 074301.

[7] Y. K. Koh, D. G. Cahill, Frequency dependence of the thermal conductivity of semiconductor alloys, Phys. Rev. B 76 (2007) 075207.

[8] K. T. Regner, S. Majumdar, J. A. Malen, Instrumentation of broadband frequency domain thermoreflectance for measuring thermal conductivity accumulation functions, Rev. Sci. Instrum. 84 (6), 064901.

[9] J. Zhu, D. Tang, W. Wang, J. Liu, K. W. Holub, R. Yang, Ultrafast thermoreflectance techniques for measuring thermal conductivity and interface thermal conductance of thin films, J. Appl. Phys. 108 (9) (2010) 094315.

[10] Y. K. Koh, S. L. Singer, W. Kim, J. M. O. Zide, H. Lu, D. G. Cahill, A. Majumdar, A. C. Gossard, Comparison of the 3ω method and time-domain thermoreflectance for measurements of the cross-plane thermal conductivity of epitaxial semiconductors, J. Appl. Phys. 105 (5) (2009) 2590.

[11] Y. K. Koh, Y. Cao, D. G. Cahill, D. Jena, Heat-transport mechanisms in superlattices, Adv. Funct. Mater. 19 (4) (2009) 610–615.

[12] A. J. Schmidt, X. Chen, G. Chen, Pulse accumulation, radial heat conduction, and anisotropic thermal conductivity in pump-probe transient thermoreflectance, Rev. Sci. Instrum. 79 (11) (2008) 114902.
[13] R. M. Costescu, M. A. Wall, D. G. Cahill, Thermal conductance of epitaxial interfaces, Phys. Rev. B 67 (2003) 054302.
[14] K. T. Regner, D. P. Sellan, Z. Su, C. H. Amon, A. J. McGaughey, J. A. Malen, Broadband phonon mean free path contributions to thermal conductivity measured using frequency domain thermoreflectance, Nat. Commun. 4 (1) (2013) 1–7.
[15] A. J. Minnich, G. Chen, S. Mansoor, B. S. Yilbas, Quasiballistic heat transfer studied using the frequency-dependent boltzmann transport equation, Phys. Rev. B 84 (2011) 235207.
[16] A. A. Maznev, J. A. Johnson, K. A. Nelson, Onset of nondiffusive phonon transport in transient thermal grating decay, Phys. Rev. B 84 (2011) 195206.
[17] A. J. Minnich, Determining phonon mean free paths from observations of quasiballistic thermal transport, Phys. Rev. Lett. 109 (2012) 205901.
[18] H. Bao, J. Chen, X. Gu, B. Cao, A review of simulation methods in micro/nanoscale heat conduction, ES Energy & Environment 1 (2018) 16–55.
[19] J. Y. Murthy, S. V. J. Narumanchi, J. A. Pascual-Gutierrez, T. Wang, C. Ni, S. R. Mathur, Review of multiscale simulation in submicron heat transfer, Int. J. Multiscale Comput. Eng. 3 (1) (2005) 5–32.
[20] J. Callaway, Model for lattice thermal conductivity at low temperatures, Phys. Rev. 113 (4) (1959) 1046.
[21] G. Chen, Ballistic-diffusive heat-conduction equations, Phys. Rev. Lett. 86 (2001) 2297–2300.
[22] B.-D. N. Dao-Sheng Tang, Yu-Chao Hua, B.-Y. Cao, Phonon wave propagation in ballistic-diffusive regime, J. Appl. Phys. 119 (12) (2016) 124301.
[23] R. A. Guyer, J. A. Krumhansl, Solution of the linearized phonon Boltzmann equation, Phys. Rev. 148 (2) (1966) 766.
[24] S. Mazumder, A. Majumdar, Monte Carlo study of phonon transport in solid thin films including dispersion and polarization, J. Heat Transfer 123 (4) (2001) 749–759.
[25] D.-S. Tang, B.-Y. Cao, Ballistic thermal wave propagation along nanowires modeled using phonon monte carlo simulations, Appl. Therm. Eng. 117 (2017) 609–616.
[26] S. A. Ali, G. Kollu, S. Mazumder, P. Sadayappan, A. Mittal, Large-scale parallel computation of the phonon Boltzmann transport equation, Int. J. Therm. Sci. 86 (2014) 341 – 351.
[27] R. Yang, G. Chen, M. Laroche, Y. Taur, Simulation of nanoscale multidimensional transient heat conduction problems using ballistic-diffusive equations and phonon Boltzmann equation, J. Heat Transfer 127 (3) (2005) 298–306.
[28] Z. Guo, K. Xu, Discrete unified gas kinetic scheme for multiscale heat transfer based on the phonon Boltzmann transport equation, Int. J. Heat Mass Transfer 102 (2016) 944–958.
[29] X.-P. Luo, Y.-Y. Guo, M.-R. Wang, H.-L. Yi, Direct simulation of second sound in graphene by solving the phonon Boltzmann equation via a multiscale scheme, Phys. Rev. B 100 (15) (2019) 155401.
[30] J. Liu, C. Zhang, H. Yuan, W. Su, L. Wu, A fast-converging scheme for the phonon boltzmann equation with dual relaxation times, J. Comput. Phys. 467 (2022) 111436.
[31] W. Su, L. Zhu, L. Wu, Fast convergence and asymptotic preserving of the general synthetic iterative scheme, SIAM J. Sci. Comput. 42 (6) (2020) B1517–B1540.
[32] S. Chapman, T. G. Cowling, The Mathematical Theory of Non-Uniform Gases: An Account of the Kinetic Theory of Viscosity, Thermal Conduction and Diffusion in Gases, Cambridge University Press, 1990.

[33] F. Yang, C. Dames, Heating-frequency-dependent thermal conductivity: An analytical solution from diffusive to ballistic regime and its relevance to phonon scattering measurements, Phys. Rev. B 91 (16) (2015) 165311.
[34] S. Huberman, C. Zhang, J. A. Haibeh, On the question of second sound in germanium: A theoretical viewpoint, arXiv:2206.02769.